Full Length Article

Histidine- and glycine-functionalized cerium oxide nanoparticles: Physicochemical properties and antiviral activity

Daniela Dupkalová [a], Yuliia Kosto [a,1], Viacheslav Kalinovych [a], Anastasiia Deineko [a], Stefano Franchi [b], Jaroslava Nováková [a], Iva Matolínová [a], Tomáš Skála [a], Kevin C. Prince [b], Anna Fučíková [c], Alexander B. Shcherbakov [d], Nadia M. Zholobak [d], Nataliya Tsud [a,*]

[a] *Charles University, Faculty of Mathematics and Physics, Department of Surface and Plasma Science, V Holešovičkách 2, Prague 18000, Czech Republic*
[b] *Elettra-Sincrotrone Trieste S.C.p.A., in Area Science Park, Strada Statale 14, km 163.5, Basovizza (Trieste) 34149, Italy*
[c] *Charles University, Faculty of Mathematics and Physics, Department of Chemical Physics and Optics, Ke Karlovu 3, Prague 12116, Czech Republic*
[d] *Zabolotny Institute of Microbiology and Virology, National Academy of Sciences of Ukraine, Kyiv 03680, Ukraine*

ABSTRACT

Cerium oxide nanoparticles (CeNPs) show great promise in biomedical applications such as theranostics of various diseases, including viral infection. In this work, we synthesized bare, histidine- and glycine-functionalized CeNPs sols and characterized them using DLS, TEM and AFM imaging, synchrotron radiation-based techniques (XPS, RPES, NEXAFS). Toxicity and antiviral activity of CeNPs were evaluated using two cell lines (mouse fibroblasts L929 and monkey kidney epithelial cells MA-104) and three types of enveloped viruses (vesicular stomatitis virus VSV, bovine beta coronavirus BCoV-1 and herpes simplex virus HSV-1/2) *in vitro*. The obtained data indicate the absence of toxic effects up to the maximum concentrations of CeNPs (0.05 M), wherein the growth-stimulating action was shown for all samples. A dose-dependent antiviral effect of CeNPs was demonstrated. The effect was the most pronounced for VSV, which enters the cell by endocytosis and triggers fusion at low pH. The histidine-functionalized CeNPs were the most stable and had enhanced ability to reduce the viral cytopathic effect; their therapeutic index for VSV was >50 to 1000 depending on cell type. An attempt was made to explain the observed phenomena from the point of view of the physics of the synthesized particles and the biology of the virus-cell interaction.

1. Introduction

The scientific community has always pushed the boundaries of medicine to develop the best drugs to treat disease and provide the most efficient treatment to patients. In recent years, nanotechnology has been successfully integrated into modern biomedical research, due to its rapid development and potential benefits. Numerous studies on various bio-applications of organic and inorganic nanoparticles (NPs) have been published with the aim of exploring their application in drug delivery systems, [1–5] bioimaging [6,7] and synthesis of artificial enzymes [8–10].

Important issues that determine the use of inorganic materials in nanomedicine are their activity and interaction with the biological environment. For NPs, these parameters are mainly defined by the interaction of biomolecules with the surface of these materials, and by functionalizing NPs with biomolecules, their properties can be advantageously modified, as was shown in Refs. [11,12]. The bonding of the amino acids histidine and glycine (Fig. S1, Supplementary Materials (SM)) to NPs is relevant in this context, because of the importance of these biomolecules for the human body. Furthermore, several studies have already been carried out on histidine- [13–15] and glycine- [16,17] functionalized NPs for biomedical applications. The principal requirements for NPs in medical use are biocompatibility and nontoxicity, which were confirmed for cerium oxide nanoparticles (CeNPs) [18,19] in a wide range of biomedical applications [4,5,10,20,21]. CeNPs are suitable for the treatment of disorders caused by oxidative stress [22,23]. In addition, CeNPs can interact with microorganisms both as a probiotic and as a bactericidal agent [24]. The antimicrobial activity of

CeO_2 colloids has been demonstrated against several groups of opportunistic microorganisms, including clinical strains of bacteria (*E. coli*, *S. aureus*) and fungi (*C. albicans*) [25]. Recently, Farias et al. evaluated antifungal activity of CeNPs against five ATCC and six clinical *C. albicans* strains, as well as their toxicity and antioxidant properties [26]. Interestingly, along with good antifungal activity, CeNPs showed low toxicity both in the *Artemia salina* model and by oral administration in mice.

One of the possible bio-applications of CeNPs is the therapy of viral diseases. Since the discovery of the antiviral activity of CeNPs by Zholobak et al., [27] the antiviral/virucidal properties of CeNPs have been intensively studied. CeNPs have been shown to protect against Indiana vesicular stomatitis virus (VSV) in cell lines of mouse fibroblasts (L929), [27,28] embryonic piglet testicles (EPT), [27] and swine testicular (ST), [29] and against herpes simplex virus 1 (HSV-1) in the normal rat fibroblasts (FR) cell line [28]. Interferon-functionalized CeNPs were shown to be an effective antiviral agent for the treatment of systemic herpetic infection [28]. Recently, the activity of biogenic CeNPs against Sabin-like poliovirus has been reported [30]. CeNPs were also discussed as a promising agent for combating the SARS-CoV-2 coronavirus and treating COVID-19 disease [31]. The virucidal activity of CeNPs has been confirmed against six viruses, including coronavirus SARS-CoV-2, transmissible gastroenteritis virus TGEV, encephalomyocarditis virus EMCV, and influenza virus (A/WSN/1933) in VERO E6, ST, BHK-21, and MDCK-2 cell lines, as well as against two bacteriophages: enveloped phi6 (DSM21518) and non-enveloped MS2 (DSM21428) in their respective host bacteria, *Pseudomonas* sp. (DSM21428) and *Escherichia coli* (DSM5695) [32]. Besides the direct antiviral activity, CeNPs increase immunogenicity of the influenza vaccine, [33] and seem to be an effective drug carrier and adjuvant in antiviral therapy [21].

In the recent work of Nefedova et al., CeNPs were shown to demonstrate enhanced virucidal activity against enveloped viruses, while the sensitivity of non-enveloped viruses towards CeNPs was significantly lower [32]. The main step of the invasion of a host cell by the enveloped viruses is the fusion of viral and cellular membranes, [34] although the triggers of this mechanism can vary significantly between different viruses. The endosomal pathway of the fusion is driven by viral surface proteins that undergo conformational rearrangements, triggered by low pH in the endosomes. This pathway is typical for most enveloped viruses, in particular, it has been shown for viruses of the family *Rhabdoviridae*, *Togaviridae*, *Bornaviridae*, *Flaviviridae*, *Orthomyxoviridae*, *Arenaviridae*, *Bunyaviridae* and others [34]. VSV (*Rhabdoviridae*) represents a relatively simple case for which low pH is sufficient to trigger fusion: the invasion of the VSV occurs over a very narrow pH range, between 5.8 and 6.2; [35] this pH value is necessary for the protonation of amino acid residues of viral fusion proteins, with histidine playing the main role in changing the conformation and the fusion machinery (so-called "histidine switch") [36]. The protonated form of the imidazole (IM) ring of histidine has a pKa of about 6, thus the imino nitrogen of the IM ring is mostly protonated below pH of 6.0 (Section S2, SM).

One of the possible mechanisms of the antiviral action of CeNPs involves interference with the fusion of the virus and the host cell membranes [37]. It is well-known that clathrin-mediated endocytosis is the main pathway for invasion by some enveloped viruses (including VSV [38]) and CeNPs uptake, [21,39] wherein protein corona (sequence of amino acids) enhances endocytosis of CeNPs [40]. Endosomes are the "meeting point" of NPs and viruses, where they can interact with each other and with cell membranes, and this interaction is determined by specific acidic conditions [37]. The histidine residues are protonated and attracted by negatively charged sites in the post-fusion conformation; due to their stability, the molecules involved in the structural rearrangements leading to fusion might provide a good target for the design of antiviral agents [36,41].

The aim of the present work is to evaluate the effect of CeNPs functionalized with simple amino acids (histidine and glycine) on these processes, i.e. whether it is possible to modulate the activity and cytopathic effect of the virus by introducing CeNPs. Thus, we investigated the antiviral activity of bare and histidine- or glycine-functionalized CeNPs (Fig. 1A) against three enveloped viruses (vesicular stomatitis virus (VSV), bovine beta coronavirus (BCoV-1) and herpes simplex virus (HSV-1/2)) with different triggers of the fusion process using cell lines of mouse fibroblasts L929 and of monkey kidney MA-104 *in vitro*. The CeNPs were characterized by UV–vis spectrophotometry. The stability of the NPs colloid solutions was characterized by dynamic light scattering (DLS). Transmission electron microscopy (TEM) and atomic force microscopy (AFM) were used to determine the CeNPs size. The electronic structure of the samples was studied by a series of photoelectron spectroscopies, namely X-ray photoelectron spectroscopy (XPS) and resonant photoelectron spectroscopy (RPES), as well as near-edge X-ray absorption fine structure spectroscopy (NEXAFS).

2. Experimental

2.1. Synthesis and functionalization of CeNPs

Cerium (III) chloride heptahydrate $CeCl_3·7H_2O$ (99.9% trace metals basis), potassium hydroxide KOH, histidine hydrochloride monohydrate $C_6H_9N_3O_2·HCl·H_2O$ (≥99% purity), glycine NH_2CH_2COOH (≥99% purity) were purchased from Sigma-Aldrich. CeNPs (bare and amino acid-functionalized) were prepared as follows: 3.73 g (10 mM) of $CeCl_3·7H_2O$ was dissolved in 100 ml of water. While stirring vigorously, the prepared solution was slowly added dropwise to the 3 M KOH solution (1000 ml). After 30 min of stirring, the solution was heated to the boiling point and continued to be stirred under reflux for 3 h. The solution was then left at room temperature without stirring to allow the NPs to settle. After 24 h the sediment was separated by decantation and dispersed in 500 ml of distilled water. The precipitate was rinsed with water several times using decantation until the pH was neutral. Finally, the suspension was diluted to 200 ml and ultrasonicated for 20 min. Thus, 0.05 M sols of CeNPs were prepared and marked as sample CO.

Histidine- (CH) and glycine- (CG) functionalized CeNPs were obtained from the sample CO as follows. An equimolar amount of amino acid (523 mg of histidine hydrochloride monohydrate and 188 mg of glycine, respectively) was added to 50 ml of the sample CO. The resulting solutions were ultrasonicated for 5 min and then stirred for 2 h. After another 24 h at room temperature, the NPs were repeatedly centrifuged and dissolved in 50 ml of distilled water. Finally, the solutions were ultrasonicated for 20 min. These samples were labelled CH (0.05 M sols of CeNPs functionalized by histidine) and CG (0.05 M sols of CeNPs functionalized by glycine) (see Fig. 1A).

2.2. UV–vis

UV−vis absorption spectra of the aqueous sols were taken with an Ocean Optics QE-65000 spectrometer (Ocean Insight, Orlando, Florida, United States).

2.3. DLS

Dynamic light scattering (DLS) measurements were performed using a Malvern Zetasizer Nano ZS (Malvern Instruments, Worcestershire, UK) to determine the zeta potential (ZP) of the prepared CeNPs in aqueous environments with different pH. The CeNPs sols were prepared by dilution of 10 μl of the original CeNPs solution (CO, CH or CG) in 1 ml of deionized water (Aqual 29) with a maximum conductivity of 0.05 μS/m. The pH was adjusted using 0.2 M HCl or 0.25 M NaOH. Each sol was ultrasonicated for 15 min right before the measurement. ZP measurements were carried out using a disposable folded zeta potential capillary cell filled with the CeNPs sol at 25 °C. ZP was calculated from the electrophoretic mobility of NPs using the Smoluchowski approximation. The value of the CeNPs refractive index was set to 2.2 [42] and absorption to 0.06, which was determined before the DLS experiment using a Specord 250 spectrophotometer (Analytik Jena).
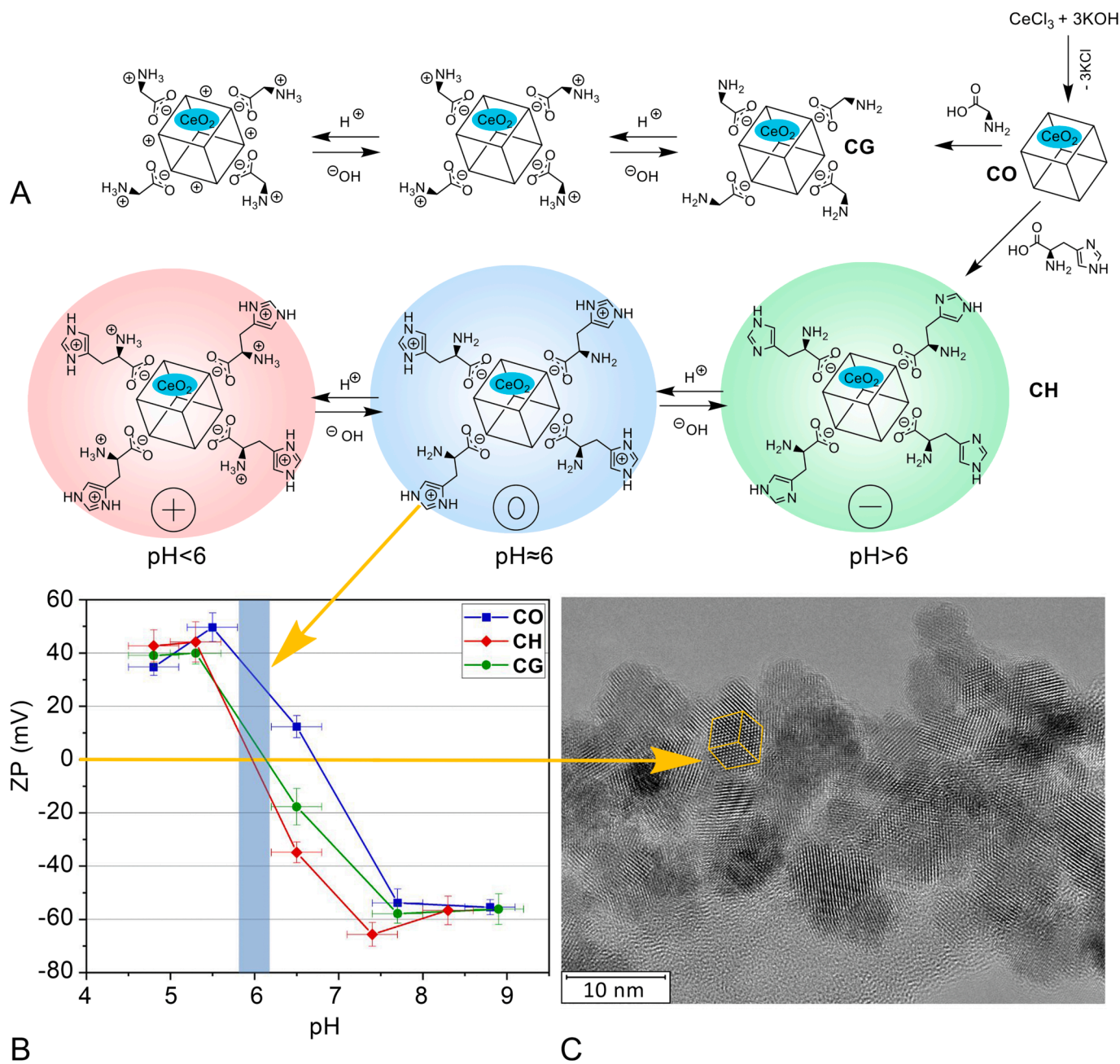
Fig. 1. Schematic view of CeNPs synthesis (CO), functionalization by glycine (CG) and histidine (CH), and their protonation at different pH (A). Zeta potential of CO, CH and CG sols in acidic, neutral and basic pH. The blue zone represents the fusion pH range of VSV in the early endosomes (B). TEM micrograph of CH nanoparticles agglomerated at the potential of zero charge; a single particle is represented by a cubic frame (C).

2.4. TEM

CeNPs were imaged by a JEOL NEOARM 200F microscope using an accelerating voltage of 200 kV in High Resolution TEM (HRTEM) mode with a resolution of 100 pm. Original CeNPs sols (sample CO, CH and CG) were ultrasonicated for 10 min and mixed with ultrapure water in a ratio of 1:50 or 1:100 (according to the optical density of the NPs sols). Then, one drop of the mixture was deposited on a carbon-coated copper grid and left to dry in air. A grain diameter of 200 to 400 NPs was measured for each sample. For several NPs in a suitable position, their interplanar distances and angles between pairs of planes were measured to determine the oxidation state of the cerium cations in the oxide.

2.5. AFM

AFM analysis was performed on a JPK NanoWizard 3 Bioscience AFM module equipped with Life Science Stage and inverted optical microscope Olympus IX73. After the agitation of the original sols, 2–8 μl of each solution was mixed with 1 ml of water (Aqual 29) and the samples CO, CG and CH were prepared and then ultrasonicated for 10 min. Samples with acidic or basic pH were prepared by the dilution of the original CeNPs sols in a ratio of 10 or 20 μl (for basic or acidic samples, respectively) to 1 ml of water, followed by the pH adjustment using 0.25 M NaOH or 0.2 M HCl as titrants. The resulting solutions were ultrasonicated for 10 min and left to stabilize for approximately 60 min. Then, 2 μl of the solution were dropped on freshly cleaved atomically flat mica support (area approximately 1 cm^2) and left to dry in air.

2.6. XPS, RPES and NEXAFS

CeNPs were characterized by synchrotron-based spectroscopies (XPS, RPES and NEXAFS) performed at the Materials Science Beamline (MSB), Elettra synchrotron, Trieste. For further details about the end station of the MSB beamline see Refs. [43,44].

Neutral samples were prepared by mixing the original CeNPs solutions (CO, CH and CG) with Milli–Q water in a ratio of 1 to 4. Acidic and basic samples were prepared by adding several μl of 0.2 M HCl or 0.25 M NaOH, respectively, to the neutral samples. Final solutions were ultrasonicated for 10 min and then 5 μl of each solution was dropcast on an unpolished glassy carbon (GC) substrate and left to dry in a desiccator. The substrate was previously cleaned in vacuum by several cycles of annealing at 200 °C followed by the Ar^+ sputtering for 15 min. Samples were prepared just before the measurements in ultra-high vacuum (10^{-10} mbar).

The C 1s, N 1s and O 1s core level spectra were recorded using synchrotron radiation (SR) with photon energies of 410, 490 and 630 eV with total resolutions of 0.42, 0.44 and 0.58 eV, respectively. The valence band (VB) spectra for RPES were acquired at photon energies of 115, 121.4 and 124.8 eV, with a total resolution of 0.2 eV (see Fig. S5B, SM). The VB spectra measured with photon energies 121.4 and 124.8 eV correspond to the emission from Ce 4f states (binding energy (BE) 1.7 eV; resonant enhancements in Ce^{3+}) and hybridized oxygen-cerium states (BE 4.2 eV; resonant enhancements in Ce^{4+}), respectively [44]. The VB spectrum acquired at the photon energy of 115 eV corresponds to off-resonance of both cerium cations and was used as a reference spectrum for the calculation of resonance enhancements $D(Ce^{3+})$ and $D(Ce^{4+})$. The resonance enhancement ratio (RER) is then calculated as $D(Ce^{3+})/D(Ce^{4+})$ from the corresponding RPES spectra (Fig. S5B, SM) and indicates the oxidation state of the cerium ions at the sample surface (information depth about 0.5 nm) [44]. Al Kα radiation from the X-ray source was used to acquire Ce 3d core level spectra with a total resolution of 1 eV. The emission angles between the sample normal and the direction to the analyser were 0° and 20° for the SR and the X-ray source, respectively. NEXAFS N K-edge spectra were measured in partial Auger yield, while Ce $M_{4,5}$-edge and O K-edge spectra were obtained from the partial yield of secondary electrons signal. The incidence of the photon beam with respect to the surface was 30°, which coincides with normal emission (NE) for photoelectrons. The energy resolution was estimated to be 0.42, 0.65 and 1.55 eV for N K-edge, O K-edge and Ce $M_{4,5}$-edge NEXAFS spectra, respectively. The SR polarization is assumed to be between 80 and 90 % linear.

PES and NEXAFS data were processed using the software KolXPD 1.8.0. The photon energy was calibrated by reference measurements of the Fermi edge on a clean Ta holder. All SRPES and NEXAFS spectra were normalized to the photon beam intensity measured using a high transmission gold mesh during the acquisition of spectra. Subtraction of the background was applied to SRPES and XPS data. From the acquired CH and CG N K-edge spectra, the corresponding background signal of the sample CO with the same pH recorded under identical conditions was subtracted.

2.7. Toxicity of the CeNPs to cell cultures in vitro

The bioapplicability of CeNPs was assessed using the reference cell line of mouse fibroblasts (L929, ATCC® CCL-1™) from the Museum of Cell Cultures of the Kavetsky Institute of Experimental Pathology, Oncology and Radiobiology, National Academy of Sciences (NAS) of Ukraine, and epithelial cell line from the kidney of an African green monkey grivet *Chlorocebus aethiops* (MA-104 cell line, ATCC® CRL-2378.1™). To form a cell monolayer, 0.1 ml of a suspension containing 5×10^5 cells/mL was added to the wells (96-well plates, Costar, USA) and incubated for 24 h at 37 °C in a TC-80 M2 thermostat (98% humidity, 5% CO_2). The growth medium used was synthetic nutrient medium DMEM/F12 (Sigma, USA), containing 8% fetal calf serum (Sigma, USA),

25 mM HEPES, 10 mM glutamine, gentamicin and canamycin (100 units/mL each). After 24 h of cultivation, the state of the monolayer of cells in the plates was monitored using an inverted light microscope. Plates with a confluent cell monolayer were used for research. The maintenance medium consisted of medium DMEM/F12, 2% fetal calf serum, 25 mM HEPES, 10 mM glutamine, gentamicin and canamycin (100 units/mL each). For washing the cell monolayer, medium DMEM/F12 without serum was used.

The samples of CeNPs were suspended in distilled water by serial double dilution, transferred to the maintenance medium in a 96-well plate (100 μl) with a confluent cells monolayer in a ratio of 1/10 (v/v), and kept together for 24 h at 37 °C in humid air (98%) containing 5% CO_2.

2.8. Crystal violet assay of CeNPs

Crystal violet (CV) assay is a simple, non-enzymatic test to quickly analyze the number of viable adhesive cells [45]. The analysis takes advantage of the affinity between the dye and the outer surface of the DNA double helix. The amount of dye absorbed depends on the total DNA content in the culture and allows us to estimate the number of viable cells. The use of the CV assay avoids possible false results in the case of direct influence of the studied substances on the mitochondrial activity and production of active oxygen forms [46].

At the end of the exposure period, the culture medium was removed and 0.5% CV solution in 30% C_2H_5OH (100 μl/well) was added. The cells were stained for 10 min at room temperature. The dye was removed, and the cells were carefully washed with water to completely remove the excess of unbound dye, the plates were dried, and 0.1 ml 70% C_2H_5OH was added to the wells to the painted adherent cells to dissolve the dye [45]. Plates were shaken for 5 min, placed in a Thermo/LabSystems Multiskan MS Microplate Reader with a vertical beam, and the absorbance was then read colorimetrically at 540 nm. Each experiment was repeated three times, with four replications. The percentage of adherent viable cells in the experimental wells was determined by the formula $(OD_{exp}/OD_{contr}) \times 100\%$, where OD_{exp}– optical density of experimental holes, OD_{cont}– optical density in control wells. In the study, intact untreated cells were used as a control.

Statistical treatment of the data obtained was performed using Bio-Stat 2009 Professional 5.8.1 software in accordance with standard recommendations. Control cells were considered to have 100% viability. Experimental data were presented as the median and the interquartile range Me (LQ–UQ), where Me – median (50% percentile), LQ – 25% percentile, UQ – 75% percentile. In the entire series, the number of experiments conducted was five.

2.9. Viruses used in the study

Vesicular stomatitis virus (VSV, Indiana strain, *Rhabdoviridae*) was used from the collection of viruses at the Zabolotny Institute of Microbiology and Virology, NAS of Ukraine, Kyiv, Ukraine. An infective titer of the virus not lower than 6 lg ID50/ml (infectious dose/ml) was used to determine the antivirus action. VSV is an enveloped, negative-sense, single-stranded RNA virus characterized by high lytic activity, short reproduction period, characteristic cytopathic effect and the ability to exert a cytopathic effect on the cells used in the work.

Bovine beta coronavirus (bovine diarrhea virus – β-BCoV-1, *Coronaviridae*) was taken from the depositary of the State Scientific Control Institute of Biotechnology and Strains of Microorganisms, Kyiv, Ukraine. BCoV-1 is an enveloped, positive-sense, single-stranded RNA virus [47]. A total of 10 passages of the virus were carried out on the MA-104 cell culture, and a virus with an infective titer 6.5 lg ID_{50}/ml (50% infectious doses per ml) was used in the work.

Herpes simplex virus 1/2 (HSV-1/2, *Herpesviridae*, double-stranded linear DNA virus deposited in the collection of viruses at the Zabolotny Institute of Microbiology and Virology, NAS of Ukraine, Kyiv,

Ukraine) with an infective titer of the virus not lower than 5 lg ID_{50}/ml was used to determine the antivirus properties of CeNPs.

For infection, 100 $TCID_{50}$ (50% tissue culture infectious dose) per ml of the corresponding viral suspension was added to the cells used in the study.

2.10. Antiviral effect of CeNPs in vitro

The studied CeNPs were introduced into cells 40 min after infection with RNA-containing viruses and 60 min after HSV-1/2 infection, i.e., at the stage when irreversible adsorption of the virus on the cell surface took place [48].

At the end of the exposure period, the virus-containing suspension was removed from the wells, CeNPs of different concentrations (0.06–4.0 mM) in a supporting medium were added to the cell mono-layers (0.1 ml per well), and cells were incubated at 37 °C for 24 h. The virus-induced cytopathic effect was investigated 24–48 h after infection. The protective effect of CeNP on a monolayer of virus-infected cells was assessed using CV assay as described above. For the control intact cells, the cell monolayer remained at 0% of cytopathic effect, i.e., 100% viable. The percentage of viable cells in experimental wells was determined according to the above-described formula for toxicity testing: $(OD_{virus}/OD_{contr}) \times 100\%$, where OD_{contr} is the optical density of intact cells stained with crystal violet; OD_{virus} is the optical density of virus-infected cells stained with crystal violet; statistical treatment of the data obtained was performed as described above.

2.11. Cell metabolic activity assay of CeNPs

Cell metabolic processes *in vitro* were studied by colorimetric technique with (3-(4,5-dimethyl-2-thiazolyl)-2,5-diphenyl-2H tetrazolium bromide (MTT assay [45]). 2 h before the end of the exposure period, the culture medium was removed from plates with a confluent cell mono-layer, and MTT solution (Sigma-Aldrich) in PBS (0.1 mg/ml, 100 μl/well) was added to the cells. After the completion of the exposure period, the supernatant liquid was removed, and a lysis solution containing 0.1% SDS (Sigma-Aldrich) solution in DMSO (Sigma-Aldrich) was added. Plates were shaken for 5 min and placed in a Thermo/LabSystems Multiskan MS Microplate Reader, and the absorbance was read calorimetrically at 492 nm. Each experiment was repeated three times with four replications.

2.12. Effect of CeNPs against reactive oxygen species in vitro

The effect of CeNPs against reactive oxygen species *in vitro* was determined as described earlier [49]. Briefly, the samples of CeNPs of different concentrations (60 μM–4.0 mM) were added to the confluent cell monolayer in a ratio of 1/10 (v/v) after 30 min of the H_2O_2 treatment (the final concentration of H_2O_2 in each well was 0.5 mM). According to the described method, [45,46] 2 h after the application of H_2O_2 the cell metabolic activity was determined by MTT assay, and the percentage of metabolically active cells was determined as described earlier for determination of the total viability of the cells in the CV assay. The metabolic activation index (MAI) was calculated using the formula C_{MTT}/C_{CV}, where C_{MTT}, % – calculated percentage of metabolically active cells relative to control cells taken as 100%; C_{CV}, % – calculated percentage of viable cells relative to control cells taken as 100%.

2.13. Statistical analysis of the biological data

All experiments testing toxicity and antiviral activity were performed in quadruplicate on each of 3 days. Numerical data are presented as the median of the first and third interquartile intervals. EC_{10}, EC_{50}, EC_{90} (effective concentrations to inhibit the cytopathic action of the virus by 10%, 50% and 90%) values were calculated by Probit regression. Comparison of assays was made by correlation and linear regression analysis. *P* values < 0.05 were considered significant. Statistical processing was performed using the BioStat 2009 Professional 5.8.1 software package.

3. Results and discussion

3.1. CeNPs characterization

3.1.1. UV–vis spectroscopy

The UV–vis absorption spectra of CO, CH and CG sols are shown in Fig. S3A of the SM. A characteristic band of Ce^{4+} at 296–298 nm with a molar attenuation coefficient of about 3700 M^{-1} cm^{-1} is observed in the spectra. Upon modification of bare CeNPs, a minor hypsochromic shift of the absorption maximum appears, and the scattering decreases followed by an increase in the stability of the sol in the series CH > CG > CO (the histidine CeNPs sol is the most stable). Amino acids practically do not affect the shape of the bare CeNPs spectrum, which indicates their low concentration in the system. The band gap (E_g) changes insignificantly and is for the direct transition 3.64, 3.66 and 3.68 eV, and for the indirect transition 3.06, 3.09 and 3.14 eV for bare, glycine- and histidine-functionalized CeNPs, respectively (see Fig. S3B,C of SM).

Bulk cerium oxide (n-type semiconductor) has a band gap (E_g) of about 3.15 eV, [50] but the value depends on the methods of material preparation and increases with the decrease of particle size [51]. The effective mass approximation theory suggests that when the material dimension decreases to reach the size of its exciton Bohr radius, the energy of the lowest excited state increases, i.e., as the nanoparticle size decreases, a blue shift occurs in optical absorption bands [52]. In our case, the individual CeNPs crystallites were 3–5 nm in size, below the Bohr radius (~7–8 nm), [53] which leads to a strong quantum confinement effect. The last is consistent with the quantum confinement model, proposed by Nie et al.: [54] band gap values can be calculated quantitatively based on CeNPs dimensions (*d*, nm) for the direct ($E_g = 3.57 + 1.28/d^2$) and indirect ($E_g = 2.99 + 2.58/d^2$) transitions. In our case for *d* of 3–5 nm these calculated values are 3.6–3.7 eV and 3.1–3.3 eV, respectively, – very close to the experimental values.

3.1.2. DLS

Zeta potential dependence of the CeNPs sols (CO, CH and CG) on the pH is shown in Fig. 1B. The measured ZP values and their standard deviations are collected in Table S4.1 of the SM. All the samples show similar behaviour. Above pH 7.5 and below pH 5.5, the sorption capacity of CeNPs is depleted, as the ZP above and below these points remains more or less constant. At these pH values, the colloid stability of the samples is quite high. At the pH of as-prepared sols (6.5), only the sample CH is quite stable with ZP of –35 mV, while the sols CO and CG show poor stability explaining their tendency to agglomerate. This result agrees well with the optical appraisal of the CeNPs sols, from which only the sample CH does not visibly settle with time.

However, amino acid surface functionalization of CeNPs has an apparent influence on their potential of zero charge (PZC), which is useful for biomedical applications (see below). According to Fig. 1B, the isoelectric point (IEP) of the bare CeNPs was found to be close to $pH_{iep} \approx$ 6.8, in good agreement with the IEP value of hydrous CeO_2 of 6.75 [55]. The specific adsorption of histidine or glycine on the surface of cerium oxide causes a shift of the PZC towards lower pH values, i.e. pH_{iep} of 6.0 or 6.15, respectively. These data may be useful in the development of CeNPs for biomedical applications. For instance, if functionalization with amino acids lowers the isoelectric point of CeNPs in the acidic direction, this may increase the affinity of NPs to the tumor cells, whose microenvironment is more acidic due to the Warburg effect. Another possible target of amino acid-functionalized CeNPs are enveloped viruses, for which fusion takes place via an endocytosis pathway in the acidic region (see blue zone in Fig. 1B) [35]. At such pH values, NPs lose their colloidal stability (first histidine-, followed by glycine-functionalized CeNPs) and are easily adsorbed on biological surfaces –

including viral fusion proteins and endosome membrane components, thus preventing virus fusion and invasion.

3.1.3. TEM

TEM micrographs of samples demonstrate well-crystallized CeNPs having small dimensions and a narrow size distribution (Fig. 1C, CH as an example); the agglomerates of individual NPs found on the grid are the result of sample drying. The data from analysis of the micrographs is shown as a set of histograms of CeNPs diameters in Fig. 2 for each sample. In general, the CeNPs are smaller than 6 nm, while a majority of the NPs have diameters of 3 to 5 nm. Most of the NPs were found to crystalize in the CeO_2 cubic structure, and very few particles have the hexagonal structure of Ce_2O_3.

3.1.4. AFM

At neutral or weakly acidic pH, CO, CH and CG sols of CeNPs tend to agglomerate, as confirmed by the AFM images shown in Fig. 3. AFM micrographs of sample CO with pH 6.5 were analysed and the histogram displaying the size distribution of NPs clusters smaller than 100 nm is shown in Fig. 4A. The very large clusters, which were the dominant ones in samples CH and CG with pH 6.5, accumulate on the dried drop border.

When the pH of the CeNPs sols is adjusted to a pH around 4.8 or 8.8, NPs agglomerates break up into smaller fragments (Fig. 3) due to higher CeNPs zeta potential and increased Coulombic repulsion between nanoparticles. This arises from the high colloid stability of the CeNPs solutions at acid and basic pH values, as follows from the DLS measurements. Straight oblique lines in the images of samples CO and CG at basic pH indicate a weak bond between the NPs clusters and the substrate. As the CH sol with pH 8.5 was prepared with a higher concentration of NPs, the formation of an incomplete monolayer was observed (Fig. 3B3) with NPs dispersed more or less uniformly (Fig. 4B). After a few days at ambient conditions, a repeated measurement showed that the layer became less uniform as the NPs slowly assembled. Therefore, it is essential to measure the drop-cast NPs layer shortly after preparation to observe its uniformity.

3.1.5. XPS and RPES

Ce 3d core level spectra (see Fig. S5A, SM) acquired at 1486.6 eV were very similar for CO, CH and CG sols in their peak positions and shapes. The spectra were fitted according to Ref. [56], as shown in Fig. S5A. From the areas of the peaks corresponding to Ce^{4+} and Ce^{3+} contributions, the averaged stoichiometry of the CeNPs within 4–6 nm of the surface [57] was found to be $CeO_{1.95}$ for all samples, which corresponds to a concentration ratio $n(Ce^{4+})/n(Ce^{3+})$ of 9. A reduction of CeNPs under X-ray irradiation, i.e. slight increase of Ce^{3+} components, was detected independently of the NPs type. It is worth noting that the stoichiometry of the NPs was estimated from the Ce 3d spectra taken at

the beginning of the data acquisition, which fairly represents the original state of cerium oxide electronic structure in the sols.

Stoichiometry of the cerium oxide on the NPs' surface was analyzed by the RPES technique, and calculating RER values [43]. Comparing the RER values at different stages of the study of one sample and also among all the samples (Table S6.1), an increase of RER with time of exposure to radiation was observed. Moreover, the RER was shown to depend strongly on the chosen spot. The extent of reduction was much higher than that observed in the Ce 3d core levels, indicating surface reduction by X-rays.

The typical C 1s core level spectra, from CH sols for instance, measured with photon energy 410 eV are shown in Fig. 5B. A dominant peak around 284.5 eV arises mainly from the GC substrate. The carbon intensity is attenuated compared to the signal from the clean GC substrate (not shown), that reflects the presence of the NPs film on the substrate. Histidine or glycine carbon atoms, except the one in the carboxyl group, contribute to the high BE part of this peak at about 286 eV [58,59]. As the molecular signal expected at 286 eV is not well defined, the BE difference between the two components of the C 1s peak from histidine and glycine functionalized NPs cannot be interpreted. The low intensity C 1s component at BE 289.0 eV arises from the carboxylate carbon atom in the molecules (in case of functionalized CeNPs) [60] and from the contamination by organic acids in ambient conditions (mainly for bare CeNPs).

O 1s core level spectra measured with photon energy 630 eV are shown in Fig. 5A1, A2 and A3 for sols CO, CH and CG, respectively. Peak O_L at the BE of 529.7 eV arises from the lattice oxygen, i.e. oxygen atoms of the cerium oxide crystal lattice. The band between 530.5 and 533.5 eV indicates the presence of adsorbed $–OH^-$ groups and H_2O on the surface. The carboxylate oxygen atoms of histidine or glycine contribute to this feature as well [58,61]. The highest intensity of the signal from $–OH^-$ (H_2O) groups is observed for the sols with basic pH, as expected in the basic environments with high concentration of the $–OH^-$ groups. High intensity in the $–OH^-$ (H_2O) region of O 1s was also observed for the sample CH at pH 4.8 but with slightly different shape. Under the assumption that the typical BE of the $–OH^-$ and H_2O species is about 531 and 532.5 eV, respectively, the H_2O component is higher compared to the $–OH^-$ signal. Moreover, their ratio, i.e.·H_2O to $–OH^-$ signals, is the highest with respect to sols (CO, CH and CG) at basic pH. We assume, that the positive charge of CH CeNPs at pH 4.8, with all three nitrogen atoms protonated (see Fig. 1A), strongly attracts the $–OH^-$ groups in the solution. These are forming adsorbed water molecules, which remained on the surface after drying of the CH drop on the GC surface. Interestingly, the effect is more pronounced for sample CH in comparison to CO and CG sols at acidic pH. We tentatively link this discrepancy to the higher number of protonated nitrogen atoms in histidine (3 N atoms) with respect to glycine (1 N atom) or clean NPs at acidic pH.

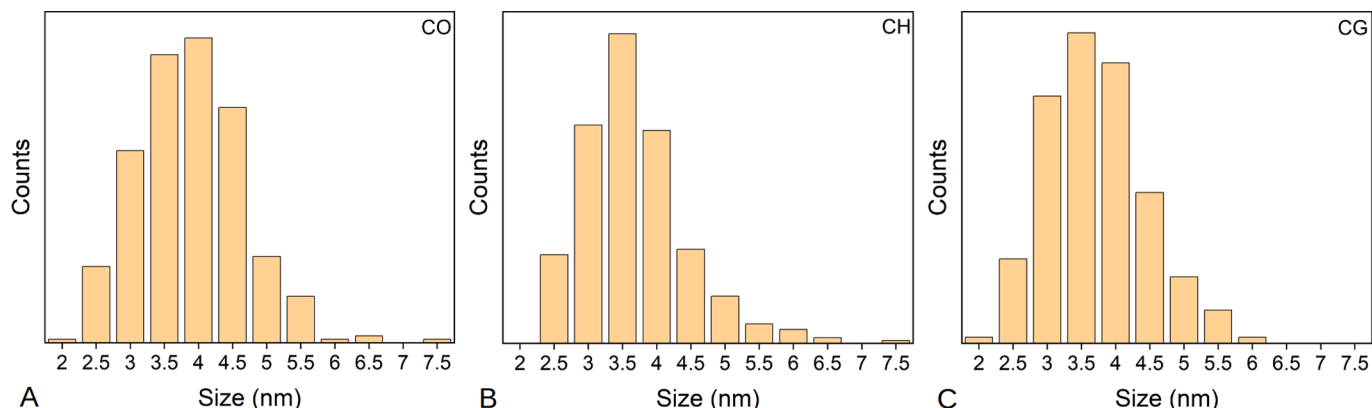While measuring the N 1s spectrum, we observed differential

Fig. 2. Histograms of particle sizes of CO (A), CH (B) and CG (C) sols measured by TEM.
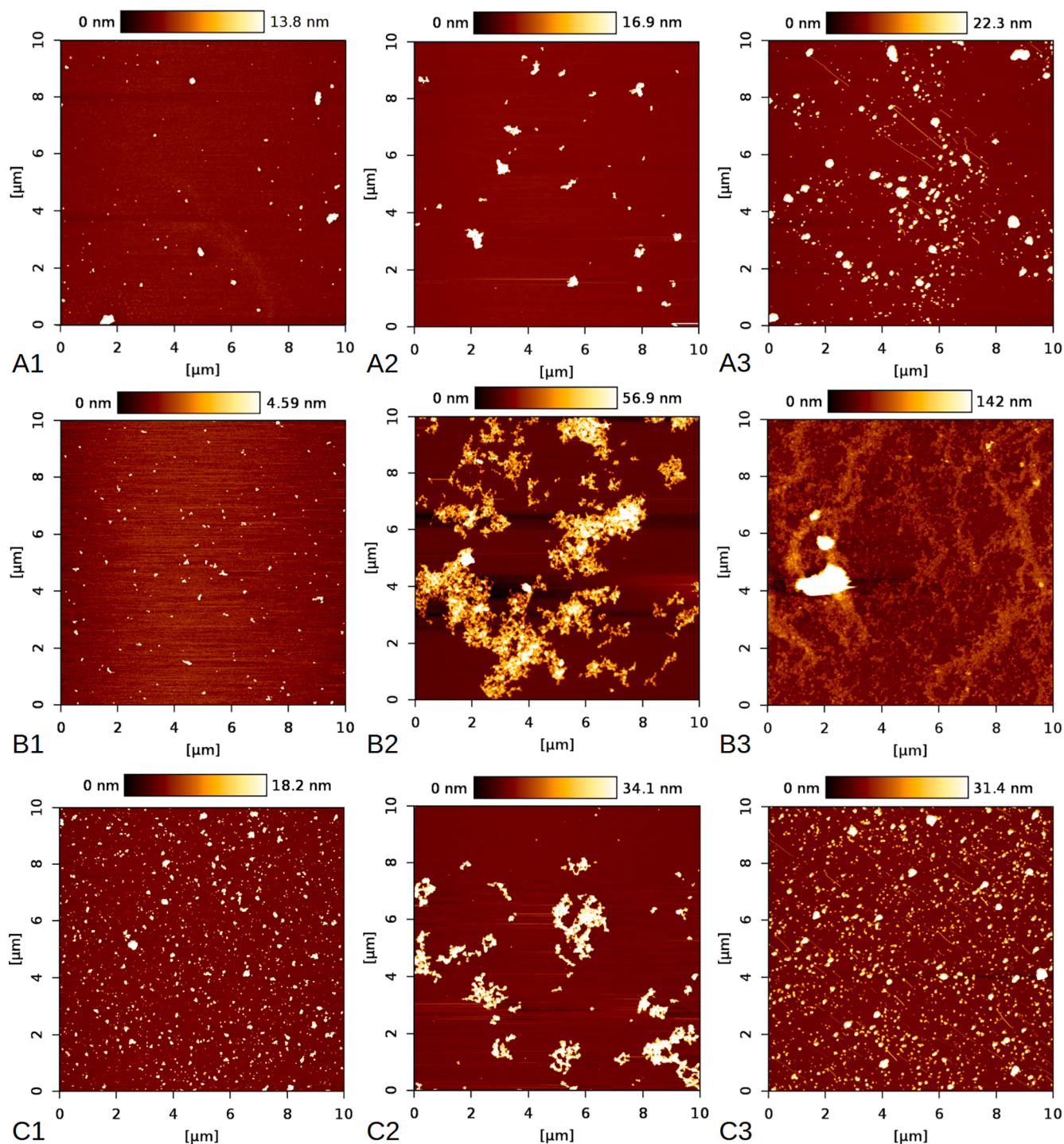
Fig. 3. AFM images of sample CO with pH 4.8 (A1), 6.5 (A2) and 8.8 (A3), sample CH with pH 4.8 (B1), 6.5 (B2) and 8.5 (B3), and sample CG with pH 4.8 (C1), 6.5 (C2) and 8.9 (C3).

charging of the CeNPs functionalized by biomolecules. Interestingly, the charge compensation for CeNPs and for the molecules adsorbed on the surface of CeNPs was different. An example of the successfully acquired spectra of CH sols, in which the N 1s peak is distinguishable, is shown in Fig. 5C1. The N 1s core levels from CG sols are shown in Fig. 5C2. At neutral pH, we were not able to measure the N 1s peak of CG sols at all (Fig. 5C2). As follows from the DLS and AFM results, at pH around 4.5 and 8.5 more uniform layers of NPs deposited on the substrate and therefore also better charge conduction can be expected. This approach proved to be useful for sample CH (at pH 8.7 and 4.8) and also for sample

CG at pH 8.9 (Fig. 5C1,C2). For these samples, the spot without charging on CeNPs was found quite easily (this applies also for sample CO at basic and acidic pH), and even the charging of the molecular adlayer was insignificant. However, a change of the pH of sample CG to pH 4.3 did not help to observe the N 1s peak, but at least helped to eliminate charging from the cerium oxide surface. It can be noticed that the spectra in which the N 1s peak is clearly visible correspond to O 1s spectra with the higher signal from –OH⁻ groups (Fig. 5A1-A3). It seems that adsorbed –OH⁻ groups in the CeNPs system improve the local conductivity of the films used for photoemission experiments.
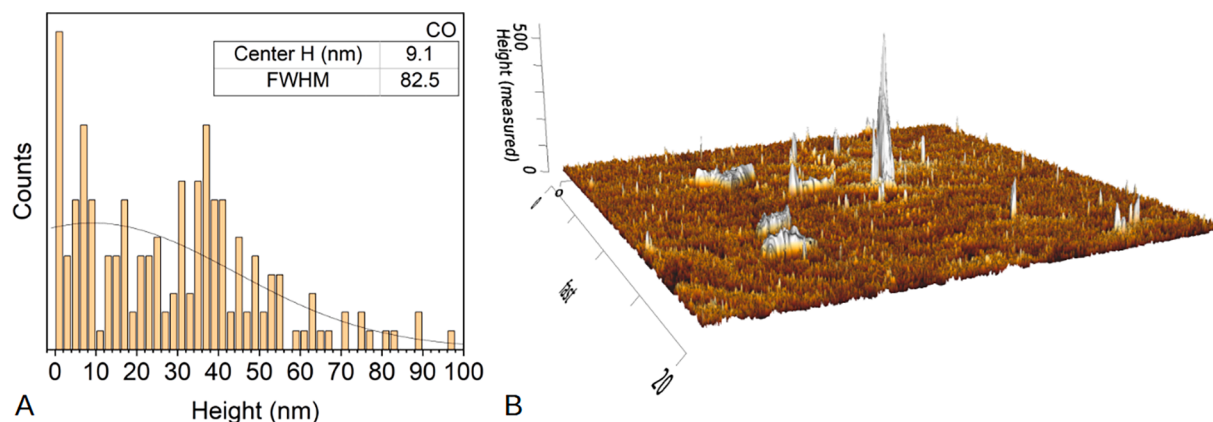
Fig. 4. Size distribution of the CeNPs clusters of the samples CO at neutral pH (A), AFM image 20 × 20 μm of sample CH with pH 8.5 in side view (B).

N 1s core level spectra were analyzed and fitted for CH, as shown in Fig. 5C1. In the N 1s spectrum of the sample CH at pH 6.7, the feature *A* at 400.4 eV corresponds to amino nitrogen of the IM ring, and the feature *B* at 399.1 eV to imino nitrogen of the IM ring and α-amino nitrogen engaged in hydrogen bonding with the surface or another molecule [60]. The intensity ratio of components *A* to *B* is about 3 to 4, in good agreement with the published data on the histidine adlayer on polycrystalline CeO_2 films, [60] where the strong bonding of the molecular adlayer to the oxide surface was observed exclusively via the carboxylate group. The feature *A* is shifted to slightly lower BE for the CH sols at pH 8.7, which indicates a change of chemical environment of the amino N atoms of the molecule. Also, the relative intensity of the component *A* is higher compared to the peak *B* with an *A* to *B* ratio of 7 to 4. Thus, the environment enriched by − OH^- affects the intermolecular hydrogen bonding and in this case amino nitrogen atoms (marked N1 and N2 in Fig. S1, SM) contribute more to the component *A*. This observation indirectly confirms the fact that amino nitrogen atoms are not involved in bonding to the CeNP at pH 8.7, which is the same scenario as for pH 6.7. Moreover, the component *B* of N 1s confirms the presence of the imino nitrogen in the IM ring (Fig. 1A), in agreement with the expected ionic forms of histidine shown in Fig. S2 and Table S2.1 of the SM. The absence of feature *B* in the spectrum of the sample CH at pH 4.8 indicates that all nitrogen atoms of histidine are protonated. Thus, the nitrogen atoms of the histidine molecule directly reflect the change of the relative concentration of H^+ and − OH^- ions in the solution, which is a sign of missing or very weak interaction with the surface of CeNPs.

For the CG sols at various values of pH (Fig. 5C2), it is apparent that the N 1s core level spectra were successfully acquired only at pH 8.9. This spectrum confirms first of all the presence of the glycine molecule on the surface of the CeNPs. The single component peak *C* in the N 1s spectrum corresponds to the amino nitrogen atom of glycine. Comparison with data on a closely related system (glycine adlayers on polycrystalline CeO_2) [59] allows us to conclude that the nitrogen of glycine is protonated and the amino group does not bond strongly with the surface.

3.1.6. NEXAFS

Neither the Ce $M_{4,5}$-edge nor the O K-edge NEXAFS spectra show visible differences in position and shape of the features for different samples. Examples of both spectra for CO sols are shown in Fig. 6A and 6B, respectively. Features marked with *F* and *G* in the Ce $M_{4,5}$-edge spectra correspond to signal from Ce^{3+} and Ce^{4+} states, respectively. Subscripts *1* and *2* denote characteristic features for the Ce M_5-edge ($3d_{3/2} \rightarrow 4f_{5/2}$ transition) and Ce M_4-edge ($3d_{5/2} \rightarrow 4f_{7/2}$ transition), respectively [62]. The spectra correspond well to previous studies and confirm that CeNPs are mainly in the form of CeO_2 with a minor concentration of the Ce_2O_3 phase, in good agreement with the $CeO_{1.95}$ film

stoichiometry estimated by analysis of the Ce 3d core level spectra.

Features in the O K-edge spectrum marked *K*, *L* and *M* at photon energies 530, 533 and 537 eV correspond to π* resonances typical for CeO_2. The feature *K* arises from excitation of the O 1s electron to hybridized Ce $4f^0$ − O 2p lowest unoccupied states. Features *L* and *M* are assigned to excitation of the O 1s electrons to hybridized Ce 5d − O 2p levels, which are split by the crystal field into two distinctive features [63]. A broad peak at photon energy 544 eV marked as *N* corresponds to 1s → σ* resonances. Almost identical shape and intensity of the oxygen absorption spectra among all samples confirm 1) the bulk origin of the signal, i.e. from the core of the CeNPs, and 2) expected unresolved features from the molecular adlayers on CeNPs mainly due to the low coverage.

The NEXAFS N K-edge spectra of samples CH and CG are shown in Fig. 6C1 and C2, respectively. Partial charging was observed for the CG sols at pH 6.7 and 4.3, the systems for which the N 1s photoelectron spectrum could not be acquired. Other spectra were considered of good quality as the typical regions of π* and σ* resonances were easily distinguishable. Features marked *P* and *R* at 400 and 402 eV for the CH sols correspond to the π* resonances of the imino and amino nitrogen atoms of the IM ring, respectively [58]. Broad peaks around 407 and 413 eV marked *S* and *T* are assigned to 1s → σ* resonances of all nitrogen atoms of histidine. The presence of two features attributed to π* resonances confirms the existence of two inequivalent nitrogen atoms in the IM ring. In the spectrum of the CH sols at pH 6.7, the intensities of the features *P* and *R* are practically equal. The last spectrum, together with the corresponding N 1s core level spectrum closely resemble the spectral features obtained for histidine adlayers on the polycrystalline cerium oxide films, [58] where molecular bonding solely through the carboxylic group was demonstrated. Thus, we can conclude that the histidine molecule is bound to the CeNPs at neutral pH in the same way as to CeO_2 polycrystalline film. At pH 8.7, the feature *P* is very weak (in line with the low intensity of the component *B* of the N 1s core level spectrum), which might indicate some charge redistribution in the ring due to the basic environment. Again, as for the N 1s results, we can indirectly confirm that the IM ring is not involved in the bonding to the oxide surface. At pH 4.8, the feature *P* vanished completely, which is due to the protonation of the imino nitrogen of the IM ring, as expected below pH 6 (Fig. S2 and Table S2.1 of SM) and in agreement with the N 1s results. Thus the π* resonance structure of the N K-edge spectrum reflects the change of pH for each sample and for the case of neutral solution, we have a direct relationship to the published reference system [60]. We conclude that the IM ring is not engaged in the bonding of histidine to the CeNPs surface at any value of pH, and the interface with the oxide is formed exclusively via the carboxylate group.

Spectra of the CG sols at pH 6.7 and pH 4.3 do not correspond to the expected spectral shape according to model systems, [59,61] as mentioned above. We do not observe σ* resonances, which are expected
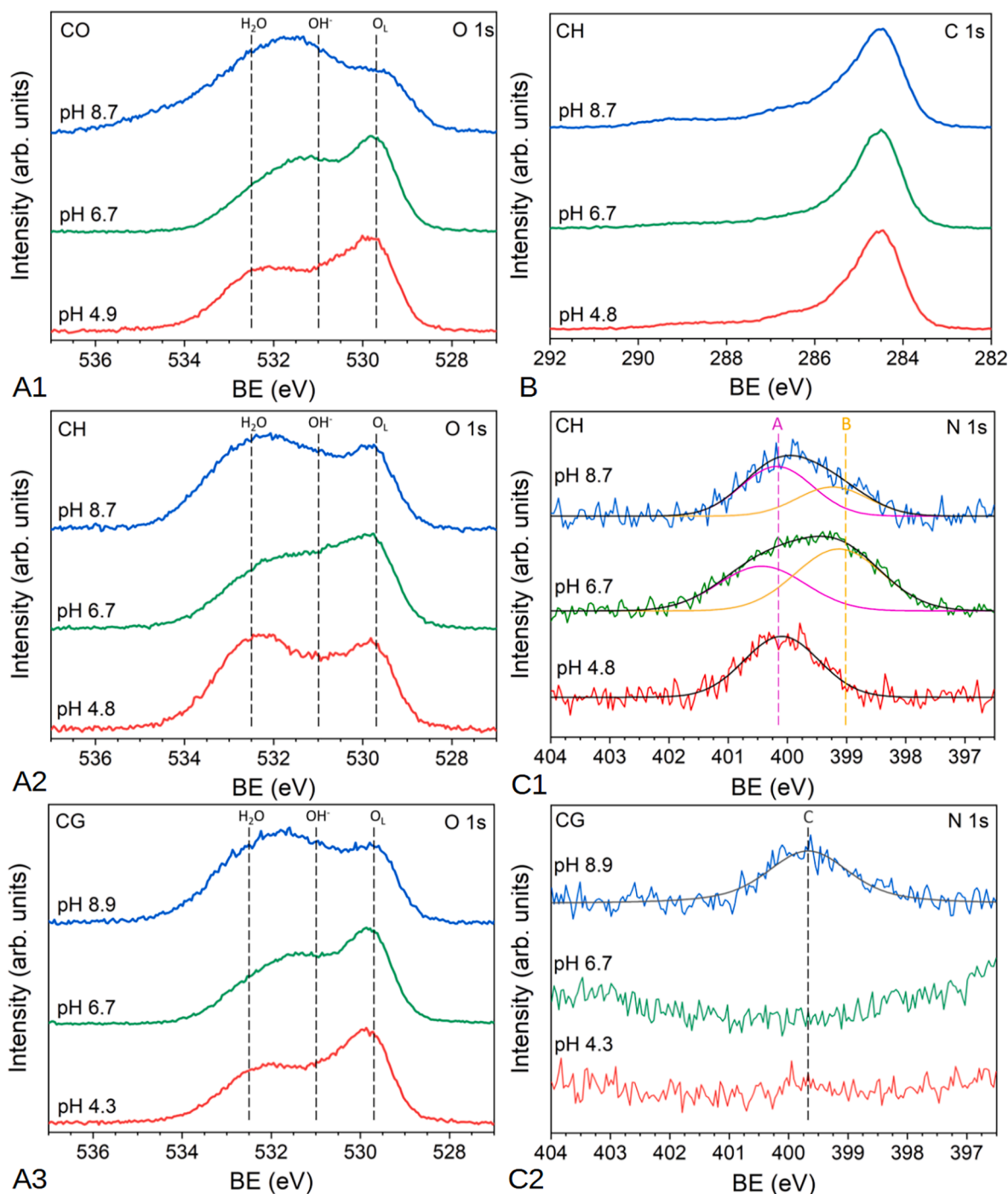
Fig. 5. O 1s core level spectra of the samples CO (A1), CH (A2) and CG (A3); C 1s core level spectrum of the sample CH at various values of pH (B); N 1s core level spectra of the samples CH (C1) and CG (C2).

around the marks *Y* and *Z*, due to the presence of charge in the molecular adlayer. At pH 8.9, σ* resonances are visible in the spectrum, but there is no peak around 400 eV (feature *X*) corresponding to π* resonances of amino nitrogen. This is in good agreement with previous results from model systems where the π* resonance feature was very low or missing at 25 °C, [59,61] and which is expected because the amino group of glycine does not have a double or triple bond. Thus, the molecular structure of glycine is likely to have a free amino group (or weakly bound by hydrogen bonds) and carboxyl oxygen atoms bound to cerium cations on the surface of the NPs.

Summarizing the characterization of the CeNPs we reach the following conclusions. According to the DLS data, the stability of CeNPs

sols strictly depends on environmental pH, wherein amino acid-functionalized CeNPs agglomerate and sediment in weakly acidic pH, which correspond to the conditions of VSV fusion, and thus can block the viral invasion via the endosomes. ZP measurements demonstrated the ability of this effect to decrease following the pattern: CH≥CG≫CO (Fig. 1B). On the other hand, in the acidic endosomal media positively-charged CeNPs can block conformation processes due to electrostatic interaction with negatively-charged sites of the VSV fusion protein; the strength of this effect in the early endosome environment decreases as follows: CO≫CG≥CH (Fig. 1B). These two pH-dependent processes can compete, so that either bare or functionalized CeNPs might make a major contribution to antiviral properties.
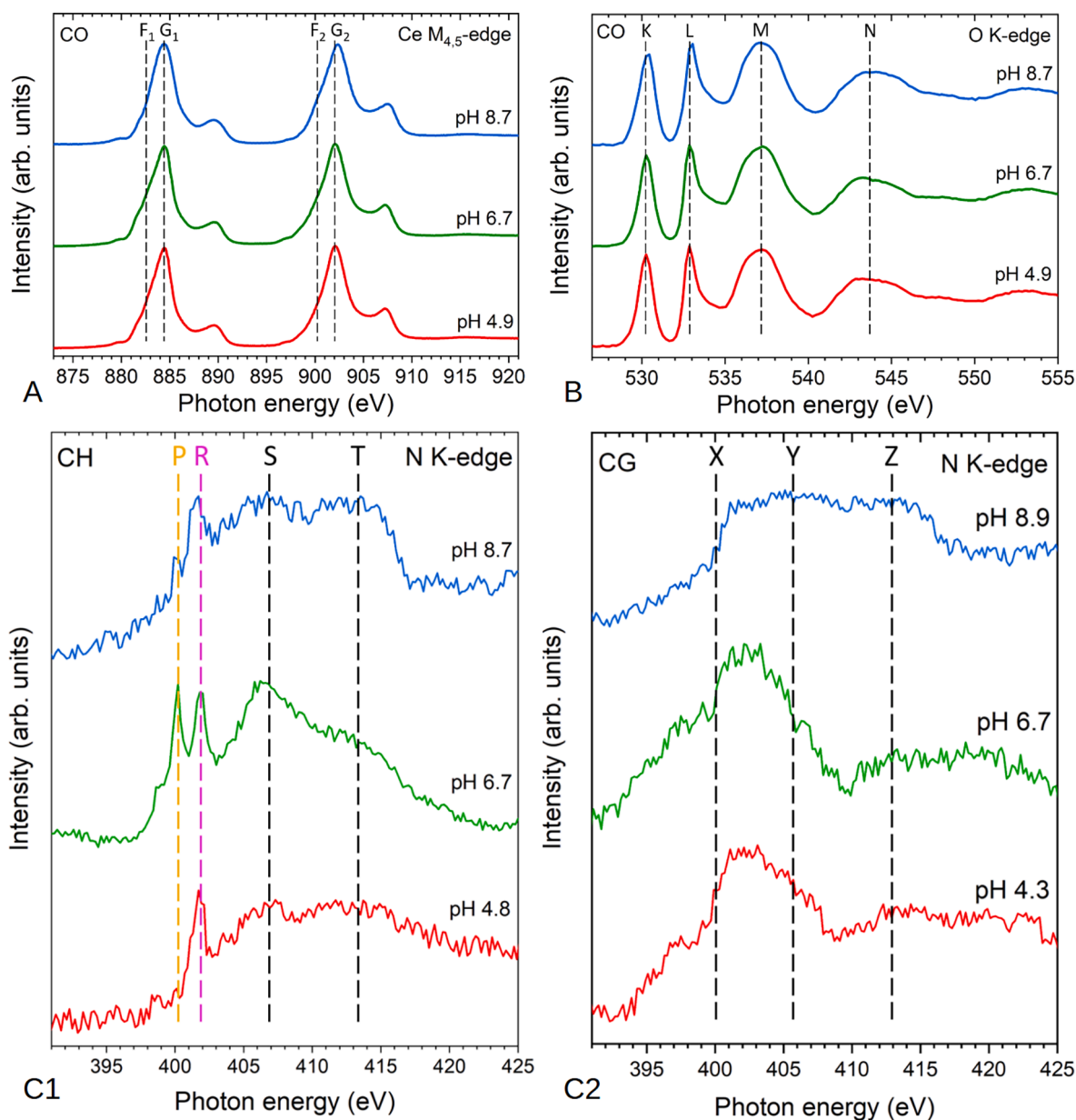
Fig. 6. NEXAFS Ce $M_{4,5}$-edge (A) and O K-edge (B) spectra of the sample CO; NEXAFS N K-edge spectra of the samples CH (C1) and CG (C2).

According to our XPS and NEXAFS results, both bare and functionalized CeNPs consist of almost pure CeO_2 with a low content of Ce^{3+} cations (about 10%) due to unsaturated bonds and grain boundaries. Thus, the observed antiviral activity is due to ceric oxide nanoparticles, bare or functionalized by histidine or glycine – not to cerous oxide or non-stoichiometric cerium oxide nanoparticles, or cerium ions.

According to XPS, the chemical states of the nitrogen atoms of the histidine directly reflect the change of the relative concentration of H^+ and $-OH^-$ ions in the solution, i.e. are protonated at acidic pH, which is a sign of missing or very weak interaction with the surface of CeNPs. In particular, the IM groups in the CH sample are not involved in bonding to the CeNPs, similarly to polycrystalline CeO_2 films [60]. Moreover, the formation of a hydrogen bonded intermolecular network is suppressed due to the low relative concentration of the –OH– groups in the solution. The nitrogen atom of glycine in the CG sol is protonated and the amino group is also not strongly bonded to the CeNPs surface. These findings are also confirmed by NEXAFS: the IM ring is not engaged in the bonding of histidine to CeNPs surface, independent of pH, and the interface with the oxide is formed exclusively via the carboxylate group; the molecular

structure of glycine is likely to have a free amino group (or weakly bound by hydrogen bonds) and carboxyl oxygen atoms bound to cerium cations on the surface of NPs. Thus, CH and CG at acidic pH are N-terminated with protonated nitrogen atoms being ready to interact with corresponding sites of viral proteins.

3.2. Biological studies

3.2.1. Toxicity of CeNPs

The results of CeNPs toxicity studies on two cell lines (mouse fibroblasts L929 and monkey kidney MA-104) are presented in Fig. 7A. The viability data (the total number of adhered cells after 24 h of their contact with various concentrations of CeNPs test samples) indicate the absence of any toxic effect even at maximum concentrations of NPs; moreover, growth-stimulating action is shown for all samples. The presence of CO and CG samples in the concentration range of 0.25–4.0 mM increases the total number of L929 cells by 8–10% compared to a control sample. The CH sample provokes a statistically significant ($P < 0.05$) increase of the number of cells by 5–8% compared to intact
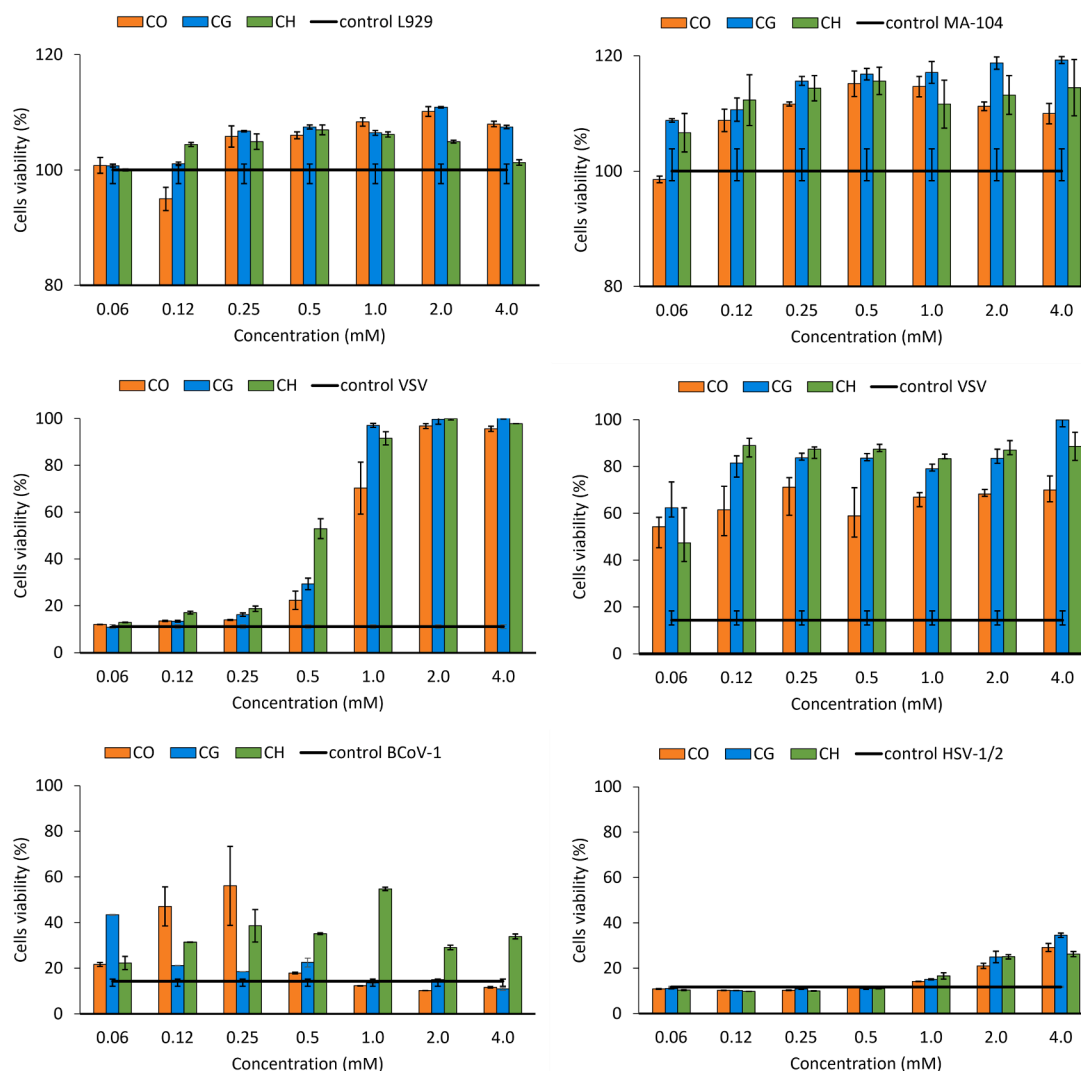
Fig. 7. In vitro toxicity and antiviral activity of the tested CeNPs. (A) – L929 (A1) and MA-104 (A2) cell viability after 24 h of contact with CeNPs monitored by CV assay. (B), (C), (D) – Antiviral activity of the CeNPs in different model systems: L929/VSV (B1), MA-104/VSV (B2), MA-104/BCoV-1 (C), MA-104/HSV-1/2 (D). Cell viability is calculated relative to control intact cells (100%).

controls in the concentration range of 0.12–2.0 mM of CeNPs. For the L929 line, the number of live cells was equal to the number of intact control cells only at the minimum tested concentration of 0.06 mM. However, even the maximum CeNPs concentration of 50.0 mM does not decrease the number of cells significantly (not shown), so the LC$_{50}$ (lethal concentration for 50% of the cell test population) value in these systems cannot be determined.

The results for the MA-104 cell line were more revealing: the sample CO showed an increase in the number of cells by 10–15% relative to a control of intact cells in the concentration range of 0.1–4.0 mM, reaching the control level at the minimum tested concentration of 0.06 mM, whereas for samples CG and CH the number of adhered cells was statistically significantly higher (P<0.05) by 7–10% than in control wells, even at the minimum concentration tested. A particularly significant concentration-dependent growth-stimulating effect was observed for the sample CG, the use of which in concentrations of 0.25–4.0 mM was accompanied by an increase in the number of adhered cells by 15–20% compared to the control. The CH sample in the concentration range of 0.1–4.0 mM caused a constant 10–15% increase in the number of cells.

Since the effect on the studied test cell lines was calculated after 24 h, i.e. in the condition that at least one cycle of cell division has passed, it can be assumed that the CO, CG and CH samples are able to influence the

growth and division of cells. In the L929 cell culture, this effect was minimal or absent in the concentration range of 0.06–0.12 mM. For MA-104 cells, the stimulant effect of cell growth and division was concentration-dependent: the maximum takes place at highest concentration, while lower concentrations lead to a reduced effect. The non-growth-promoting concentration for MA-104 cells was calculated to be 0.03 mM of CeNPs or less.

The difference in the sensitivity of cell lines to CeNPs samples is most likely due to the specificity of the exchange and metabolic rate of the cells, as well as their origin (mouse or monkey). Considering the fact that MA-104 cells are kidney line, they are characterized by the presence of Ca-sensing receptors (CaSRs), or "calcium sensor", [64] while they are absent on mouse fibroblast cells. The presence of CaSR can significantly facilitate the penetration of cerium-containing sols into the cell. We suggest it is a reason for a more pronounced stimulating effect of cerium-containing sols on the total number of MA-104 cells in comparison to the L929 line.

3.2.2. Antiviral activity of CeNPs

Most scientists have evaluated the antiviral activities of CeNPs by considering their ability to inactivate the virus through direct extracellular capsid-particle interaction, i.e. probing the virucidal property of CeNPs. Thus, in the work of Nefedova et al., [32] CeNPs have been

confirmed as a virucide under the European Biocidal Products Regulation requirements for antimicrobial efficacy testing of treated articles. Henych et al. studied virucidal effectiveness of CeNPs against enveloped (human herpes simplex) and non-enveloped (adenovirus 5) viruses based on the European standard (EN 14476). In particular, a quantitative suspension test of the disinfectants and antiseptics was used for the evaluation of CeNPs virucidal activity in the medical area (Phase 2/Step 1) [65]. Neal et al. reported on silver-decorated CeNPs inactivation of the human coronavirus OC43 and rhinovirus RV14 by surface disruption. The authors suggested that the dominant physical interaction of one type of NPs with the OC43 envelope is a disruption of the lipid bilayer, whereas another type of NPs with the RV14 protein shell inactivates the virion due to the denaturation of the proteins involved in the receptor binding [66]. Such approaches allow us to evaluate CeNPs as a disinfectant-virucide, i.e. its ability to kill germs upon direct contact. In general, the concept of virucide differs from an antiviral drug in that the latter affects the process of virus-cell interaction by suppressing the virus-induced cascade of reactions in the cell and the body. Therefore, the virucidal and antiviral properties of CeNPs against the same virus can differ significantly (for example, the study of herpesvirus by Henych at al. [65]).

The first stage of studying a substance as an antiviral drug requires an assessment of its efficiency in a culture of previously infected cells in a therapeutic regimen. Thus, we studied the therapeutic administration of CeNPs in the early stages of an actively developing infectious process.

The L929/VSV model system is a standard in virological research, for which the molecular mechanisms of virus-cell interaction are well studied. The time interval choice, 30 min after infection, is based on the well-known behavior and properties of cells infected by VSV. The virus enters the cell and starts an active infection process in the first 30 min. Thus, the selected time interval from the moment of cell infection corresponds to the beginning of intracellular virus replication. For BCoV-1, as an RNA-containing virus, the time interval of the virus penetration into the cell is similar, i.e., about 30 min. For HSV-1/2, the activation of the intracellular infectious process, caused by almost complete virus adsorption on sensitive cells, begins 60 min after infection [48]. The beginning of the development of the cytopathic effect of the HSV-1 virus in MA-104 cell culture occurs 12 h from the infection and reaches a maximum of 24–48 h after infection [67].

According to our results (Fig. 7B), maximum protection against VSV by CeNPs occurs in both cell lines. Just as in the case of the CeNPs toxicity test, different protection efficiency was observed depending on cell type. In particular, it was significantly higher for the MA-104 cells. This fact is obviously related to the increased affinity of NPs to the cells due to the presence of CaSR and enhanced endocytosis. The involvement of CaSR is indirectly confirmed by the high activity of bare CeNPs (CO), whose surface affinity for calcium receptors is higher than that of NPs functionalized by amino acids, which partially blocks the surface-active sites. In the L929/VSV system (Fig. 7B1), 100% survival of infected cells was shown at a concentration range of 2.0–4.0 mM for all tested sols. Moreover, the cell protection effect was shown to be concentration-dependent. It should be noted that the efficiency of L929 cell protection by the CeNPs has the following pattern: CH>CG>CO and is more pronounced in the low-concentration region. In the MA-104/VSV system (Fig. 7B2), 100% protection of VSV-infected cells is shown only for the sample CG at the maximum concentration. However, >50% protection of infected cells was observed for all tested CeNPs with concentration ≥0.12 mM. A decrease in protection to below 50% of adhered cells is observed only at the minimum studied concentration of 0.06 mM. The average efficiency of MA-104 cell protection by the CeNPs has the pattern CH≥CG>CO. Probably, the enhanced effect of bare CeNPs (CO) occurs due to the influence of CaSR.

In the MA-104/BCoV-1 system (Fig. 7C), 100% protection of cells from the cytopathic effect of the virus was not detected for any of the sols, although 50% cell survival was shown for CO (0.25 mM) and CH (1.0 mM). As in the L929/VSV model test system (Fig. 7B1), CH showed overall higher antiviral efficacy than CO and CG. On the other hand, it is interesting that, in contrast to the L929/VSV and MA-104/VSV model systems, the use of maximum concentrations of CO and CG samples does not provide any protection of cells against the cytopathic effect of the BCoV-1 virus. A certain protective effect is observed for CO in the range of 0.07–0.3 mM and for CG at the minimal studied concentration of 0.06 mM.

In the MA-104/HSV-1/2 system (Fig. 7D), the protective effect of the CeNPs was minimal and was detected at the level of 10% only when the samples were used at the maximum tested concentration of 4.0 mM, although for the CH sol, the minimal protective effect was observed even at 1.0 mM concentration. A summary of effective antiviral concentrations of the studied CeNPs sols added to the cells in a therapeutic regimen is given in Table 1.

All components of the model test systems contribute to antivirus protection to a different extent. As noted above, the cell lines differ both in their origin (L929 – mice and MA-104 – monkeys) and the specificity of metabolism and metabolic rate. A stable genotype, high sensitivity to infection by viruses with negative-strand RNA, and low sensitivity to infection with DNA or positive-strand RNA viruses characterize L929 mouse fibroblast line. The MA-104 epithelial cells from the kidney of an African green monkey grivet *Chlorocebus aethiops* are highly sensitive to all these viruses. In all cases, considering the scheme applied to test the CeNPs antiviral activity, for interpretation of the results, the process of penetration of the virus into the cell is very important, especially the processes of fusion and decapsidation (the destruction of viral capsid with the release of nucleic material). These processes are somewhat different for the viruses studied here.

As noted above, the internalization of VSV into the cell occurs by clathrin-mediated endocytosis. In the secondary endosomes with an acidic pH, VSV invades the cell, where it can fuse with the membrane due to the "histidine switch" mechanism, [68] causing the uncoating and releasing content into the cell cytoplasm. In the case of VSV infection, CeNPs have the highest protective effect, and amino acids (primarily histidine) make the greatest contribution. The antiviral therapeutic index (TI) of CH CeNPs (TI=LC$_{50}$/EC$_{50}$; LC$_{50}$>0.05 M, EC$_{50}$=0.03–0.5 mM) against VSV is >50 or 1000, depending on cell type.

Unlike rhabdoviruses, coronaviruses are able to enter the cell in two ways: via the same endocytosis and via the direct fusion with the cellular membrane; the last mechanism is activated by receptor binding followed by protease action [34]. The plasma membrane route seems to be dominant in the coronavirus entry ("early pathway"), while the endosomal route is a "late pathway" [69]. The antiviral effect of CeNPs in the case of BCoV-1 is less than for VSV, possibly due to the endocytic mechanism's minor contribution to the virus penetration into the host cell. Besides, launching the infectious process initiated by a coronavirus (BCoV-1) occurs faster than the rhabdovirus (VSV) because the BCoV-1 has infectious positive-sense, single-stranded RNA that serves as mRNA and has a unique replication mechanism. It is important that the entire reproduction cycle of VSV and BCoV-1 viruses occurs outside the nucleus, in the cell's cytoplasm.

Herpes viruses are enveloped viruses that fuse at neutral pH and are triggered solely by binding to a host cell multiple receptors, and endocytic mechanisms are absent [34,70]. As expected, the antiviral activity of histidine-functionalized CeNPs was less noticeable in the case of HSV. The penetration of HSV into the cell is followed by the cytoskeleton-mediated transport of the viral capsid to the nucleus, its docking with nuclear pores, where the viral DNA is released into the nucleoplasm. Thus, the key moments of HSV replication occur in the host cell's nucleus and are much more delayed. Histidine stabilized AuNPs are found to inactivate an enveloped, double-stranded DNA pseudorabies virus belonging to the family *Herpesviridae* via blockage of the viral replication process rather than the processes of attachment, penetration, or release [71]. A schematic view of the antiviral activity of CeNPs for the studied cell lines is shown in Fig. 8.

Table 1

Effective antiviral concentrations of CeNPs in mM according to the treatment *in vitro*.

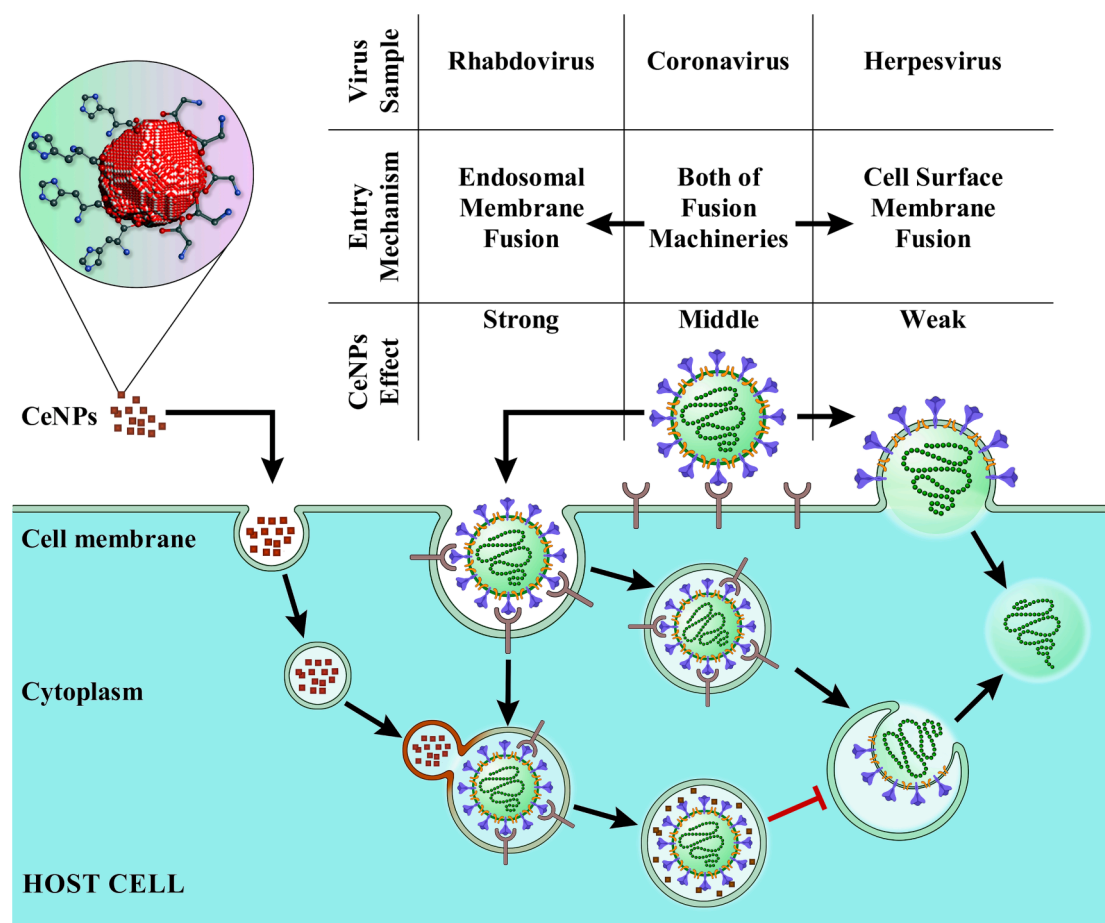| Model system	EC_{10}			EC_{50}			EC_{90}		
	CO	CG	CH	CO	CG	CH	CO	CG	CH
L929/VSV	0.75	0.5	0.3	1.0	0.8	0.5	2.0	1.1	1.2
MA104/ VSV	<0.06	<0.06	<0.06	0.06	0.02	0.03	0.12	3.0	–
MA-104/BCoV-1	0.1	0.06	0.2	0.25	–	1.0	–	–	–
MA-104/HSV-1/2	4.0	3.5	3.8	–	–	–	–	–	–

Fig. 8. Schematic illustration of a possible mechanism of CeNPs' effect on virus invasion.

Various signaling pathways are activated during the viral infection – from virus entry to apoptotic host cell death, wherein apoptosis is mainly associated with viral oxidative stress (OS). From this point of view, some (or a considerable) part of the antiviral activity of CeNPs may be caused by their ability to reduce OS and inhibit apoptosis following viral OS. To assess the antioxidant ability of CeNPs, we studied their effect on the viability and metabolic activity of MA-104 cells subjected to the cytotoxic effect of hydrogen peroxide in the therapeutic regimen of administration (CeNPs were introduced to the cells 30 min after H_2O_2). The results demonstrated low protective effects of CeNPs against exogenous reactive oxygen species (see Table S7.1 in SM). Thus, an antioxidant mechanism cannot play the primary role in the CeNPs protection from viral infection. At the same time, according to the MTT assay, the metabolic activity of cells was changed.

The activation index data can be helpful in understanding the different effects of the CeNPs concentrations under infection conditions with viruses of various systematic groups. In particular, higher metabolic activity was registered for cells treated with higher concentrations of CeNPs in the following order: CO≥CG>CH. According to the number of adhered cells, which corresponds to the total number of cells in the well, the dependence is inverse: a greater number of living cells was detected at lower concentrations of CeNPs. The protective activity of CeNPs decreased in the following order: CH>CO≥CG. It should be noted that the integral indicator, namely cell metabolic activation index (its value is 1.0 for the intact control cells), differs significantly between CeNPs: almost in the entire range of CO and CG concentrations, it is much higher than 1.0, and it is lower than 1.0 for cells treated with CH. The initial stage of a viral infection is known to be accompanied by a sharp activation of cellular metabolic processes, which provides favorable conditions for virus replication. The greater ability of histidine-functionalized CeNPs to inhibit the development of the virus-induced cytopathic effect may be associated with a decrease in the cell metabolic activity index. At the same time, the antiviral mechanisms of CO and CG cannot be explained in terms of this approach and differ from that of CH.

Carneiro et al. demonstrated that the interaction of VSV fusion peptide with the cell membrane depends on the presence of histidine residues in the peptide, [72] and these residues are protonated [73]. We

assumed that protonated histidine moieties bound to CeNPs could mimic the behavior of such residues in the viral peptide chain. At the same time, the CO sample (bare CeNPs) also possesses pronounced antiviral activity in all the studied models. In the endosomal acidic pH range of 5.8–6.2 (Fig. 1), the amino acid-functionalized CeNPs tend to agglomerate and adhere to biological surfaces within the endosome. On the other hand, bare CeNPs have the highest positive charge in this environment. The process of CeNPs accumulation can be both non-specific (due to zeta potential being near the point of zero charge of CeO_2 sols, see above) and specific (due to the histidine-binding sites on the surface of viral fusion proteins). The contribution of any given phenomenon to blocking virus invasion determines the antiviral activity of that type of CeNPs. Based on the study of antiviral ability of CeNPs with opposite surface charge, (+) and (−), Nefedova et al. concluded that the intrinsic properties of the NPs were responsible for the virucidal antiviral effects rather than surface charge or surface functional groups [32]. In contrast, we found that the presence of amino acids seems to increase the effectiveness of antiviral protection of CeNPs in some cases, but this effect is moderate. Features of the virus-cell interaction, namely the mechanisms of virus invasion into the host cell, are crucial in the antiviral activity implementation of CeNPs in the therapeutic regimen. It has been established that the CeNPs studied here possess the highest activity against VSV, an enveloped virus which infects the host cell by pH-dependent endocytosis.

4. Conclusions

The physicochemical properties of cerium oxide nanoparticles (CeNPs) – bare (CO) and functionalized with histidine (CH) or glycine (CG) – were studied using UV–vis, DLS, TEM, AFM and photoelectron spectroscopy-based techniques (XPS, RPES, and NEXAFS). The CeNPs were shown to have mostly cubic structure of nearly stoichiometric CeO_2 with crystallites of average size from 3 to 5 nm. The colloidal stability of CeNPs depends on the environmental pH: bare CeNPs agglomerate and sediment at neutral pH, 6.8–7.0, while amino acid-functionalized NPs agglomerate at pH 5.8–6.2. The chemical state of the nitrogen atoms of the histidine in the CH sol reflects the change of the relative concentration of H^+ and OH^- ions in the solution with the IM group not involved in bonding to the CeNPs and being protonated in the proton-rich environment (acidic pH). Similarly, the nitrogen atom of glycine in the CG sol is protonated and amino group is not strongly bonded to the CeNPs surface at acidic pH. For both amino acids, the interface with the oxide is formed via the carboxylate group. The initial average stoichiometry of CeNPs is $CeO_{1.95}$ for all sols. Surface reduction of CeNPs was observed under X-ray irradiation.

Two cell lines (L929 and MA-104) and three types of enveloped viruses (VSV, BCoV-1 and HSV-1/2) were used to evaluate the toxic and antiviral properties of CeNPs sols in the therapeutic regimen *in vitro*. The viability data indicate the absence of any toxicity even at the maximum concentration of CeNPs of 0.05 M. The growth-stimulating effect of CO, CH, and CG sols was observed for both cell lines. The antiviral activity of CeNPs was observed to be dose-dependent with a slight enhancement in the case of CeNPs functionalized with amino acids (CG and CH). The CH sol was found to be the most stable and had an enhanced ability to inhibit the cytopathic effect induced by the viruses. The effect is most pronounced for the vesicular stomatitis virus, which enters the cell by endocytosis and triggers fusion at low pH. The antiviral therapeutic index of CH nanoparticles against VSV was >50 to 1000 depending on the cell type, the highest compared to CO and CG sols. The antiviral activity of CeNPs has been confirmed and improved for systems functionalized with small biomolecules, where the interaction with the surface can be properly addressed.

CRediT authorship contribution statement

Daniela Dupkalová: Data curation, Formal analysis, Investigation, Writing – original draft. **Yuliia Kosto:** Data curation, Formal analysis, Investigation. **Viacheslav Kalinovych:** Data curation, Formal analysis, Investigation. **Anastasiia Deineko:** Data curation, Formal analysis, Investigation. **Stefano Franchi:** Data curation, Formal analysis, Investigation. **Jaroslava Nováková:** Data curation, Formal analysis, Investigation. **Iva Matolínová:** Funding acquisition, Writing – review & editing. **Tomáš Skála:** Data curation, Methodology, Writing – review & editing. **Kevin C. Prince:** Methodology, Writing – review & editing. **Anna Fučíková:** Conceptualization, Investigation, Methodology, Supervision, Writing – review & editing. **Alexander B. Shcherbakov:** Conceptualization, Investigation, Methodology, Supervision, Writing – review & editing. **Nadia M. Zholobak:** Conceptualization, Investigation, Methodology, Supervision, Writing – review & editing. **Nataliya Tsud:** Conceptualization, Investigation, Methodology, Supervision, Writing – review & editing.

Declaration of Competing Interest

The authors declare that they have no known competing financial interests or personal relationships that could have appeared to influence the work reported in this paper.

Data availability

Data will be made available on request.

Acknowledgements

Appendix A. Supplementary data

Supplementary data to this article can be found online at https://doi.org/10.1016/j.apsusc.2023.157793.

References

[1] J. Wen, K. Yang, F. Liu, H. Li, Y. Xu, S. Sun, Diverse gatekeepers for mesoporous silica nanoparticle based drug delivery systems, Chem. Soc. Rev. 46 (2017) 6024, https://doi.org/10.1039/c7cs00219j.

[2] X. Jiang, C. He, W. Lin, Supramolecular metal-based nanoparticles for drug delivery and cancer therapy, Curr. Opin. Chem. Biol. 61 (2021) 143–153, https://doi.org/10.1016/j.cbpa.2021.01.005.

[3] C. Lei, X.R. Liu, Q.B. Chen, Y. Li, J.L. Zhou, L.Y. Zhou, T. Zou, Hyaluronic acid and albumin based nanoparticles for drug delivery, J. Control. Release. 331 (2021) 416–433, https://doi.org/10.1016/j.jconrel.2021.01.033.

[4] L. Cao, G. Shao, F. Ren, M. Yang, Y. Nie, Q. Peng, P. Zhang, Cerium oxide nanoparticle-loaded polyvinyl alcohol nanogels delivery for wound healing care systems on surgery, Drug Deliv. 28 (2021) 390–399, https://doi.org/10.1080/10717544.2020.1858998.

[5] J.A. Vassie, J.M. Whitelock, M.S. Lord, Targeted delivery and redox activity of folic acid-functionalized nanoceria in tumor cells, Mol. Pharm. 15 (2018) 994–1004, https://doi.org/10.1021/acs.molpharmaceut.7b00920.

[6] Y. Fan, S. Liu, Y. Yi, H. Rong, J. Zhang, Catalytic nanomaterials toward atomic levels for biomedical applications: from metal clusters to single-atom catalysts, ACS Nano. 15 (2021) 2005–2037, https://doi.org/10.1021/acsnano.0c06962.

[7] Q. Ma, J. Wang, Z. Li, X. Lv, L. Liang, Q. Yuan, Q.Q. Ma, J. Wang, Z.H. Li, X.B. Lv, Q. Yuan, L. Liang, Recent progress in time-resolved biosensing and bioimaging based on lanthanide-doped nanoparticles, Small. 15 (2019) 1804969, https://doi.org/10.1002/smll.201804969.

[8] M. Pietrzak, P. Ivanova, Bimetallic and multimetallic nanoparticles as nanozymes, Sens. Actuat., B Chem. 336 (2021), 129736, https://doi.org/10.1016/j.snb.2021.129736.

[9] M. Gao, P. An, H. Rao, Z. Niu, X. Xue, M. Luo, X. Liu, Z. Xue, X. Lu, Molecule-gated surface chemistry of Pt nanoparticles for constructing activity-controllable nanozymes and a three-in-one sensor, Analyst. 145 (2020) 1279, https://doi.org/10.1039/c9an01956a.

[10] N. Feng, Y. Liu, X. Dai, Y. Wang, Q. Guo, Q. Li, Advanced applications of cerium oxide based nanozymes in cancer, RSC Adv. 12 (2022) 1486–1493, https://doi.org/10.1039/d1ra05407d.

[11] J. Yoo, C. Park, G. Yi, D. Lee, H. Koo, Active targeting strategies using biological ligands for nanoparticle drug delivery systems, Cancers (Basel). 11 (2019) 640, https://doi.org/10.3390/cancers11050640.

[12] A. Heuer-Jungemann, N. Feliu, I. Bakaimi, M. Hamaly, A. Alkilany, I. Chakraborty, A. Masood, M.F. Casula, A. Kostopoulou, E. Oh, K. Susumu, M.H. Stewart, I. L. Medintz, E. Stratakis, W.J. Parak, A.G. Kanaras, The role of ligands in the chemical synthesis and applications of inorganic nanoparticles, Chem. Rev. 119 (2019) 4819–4880, https://doi.org/10.1021/acs.chemrev.8b00733.

[13] G.R. Dhanya, D.S. Caroline, M.R. Rekha, K. Sreenivasan, Histidine and arginine conjugated starch-PEI and its corresponding gold nanoparticles for gene delivery, Int. J. Biol. Macromol. 120 (2018) 999–1008, https://doi.org/10.1016/j.ijbiomac.2018.08.142.

[14] S. Chhibber, V.S. Gondil, S. Sharma, M. Kumar, N. Wangoo, R.K. Sharma, A novel approach for combating klebsiella pneumoniae biofilm using histidine functionalized silver nanoparticles, Front. Microbiol. 8 (2017) 1–10, https://doi.org/10.3389/fmicb.2017.01104.

[15] C.N. Iswarya, S.C.G.K. Daniel, M. Sivakumar, Studies on L-histidine capped Ag and Au nanoparticles for dopamine detection, Mater. Sci. Eng. C. 75 (2017) 393–401, https://doi.org/10.1016/j.msec.2016.11.102.

[16] I. Antal, M. Koneracka, M. Kubovcikova, V. Zavisova, A. Jurikova, I. Khmara, M. Omastova, M. Micusik, M. Barathova, L. Jelenska, I. Kajanova, M. Zatovicova, S. Pastorekova, Targeting of carbonic anhydrase IX-positive cancer cells by glycine-coated superparamagnetic nanoparticles, Colloids Surf. B Biointerfaces. 205 (2021), 111893, https://doi.org/10.1016/j.colsurfb.2021.111893.

[17] C. Chen, J. Fang, C. Xu, Ultrasonication mediated fabrication of glycine coated gadolinium oxide nanoparticles as MRI contrast agents, J. Clust. Sci. 32 (2021) 773–778, https://doi.org/10.1007/s10876-020-01836-1.

[18] M.B. Khorrami, H.R. Sadeghnia, A. Pasdar, M. Ghayour-Mobarhan, B. Riahi-Zanjani, A. Hashemzadeh, M. Zare, M. Darroudi, Antioxidant and toxicity studies of biosynthesized cerium oxide nanoparticles in rats, Int. J. Nanomed. 14 (2019) 2915–2926, https://doi.org/10.2147/IJN.S194192.

[19] Y.-H. Lin, L.-J. Shen, T.-H. Chou, Y.-H. Shih, Synthesis, stability, and cytotoxicity of novel cerium oxide nanoparticles for biomedical applications, J. Clust. Sci. 32 (2021) 405–413, https://doi.org/10.1007/s10876-020-01798-4.

[20] M.J.N. Amaldoss, R. Mehmood, J.-L. Yang, P. Koshy, N. Kumar, A. Unnikrishnan, C.C. Sorrell, Anticancer therapeutic effect of cerium-based nanoparticles: known and unknown molecular mechanisms, Biomater. Sci. 10 (2022) 3671–3694, https://doi.org/10.1039/D2BM00334A.

[21] A.B. Shcherbakov, N.M. Zholobak, V.K. Ivanov, 8 - Biological, biomedical and pharmaceutical applications of cerium oxide, in: Cerium oxide (CeO2): synthesis, properties and applications (Eds.), Met. Oxides, Elsevier, 2020: pp. 279–358, doi: 10.1016/B978-0-12-815661-2.00008-6. https://www.sciencedirect.com/science/article/abs/pii/B9780128156621000086.

[22] I. Celardo, J.Z. Pedersen, E. Traversa, L. Ghibelli, Pharmacological potential of cerium oxide nanoparticles, Nanoscale. 3 (2011) 1411–1420, https://doi.org/10.1039/c0nr00875c.

[23] G. Casals, M. Perramón, E. Casals, I. Portolés, G. Fernández-Varo, M. Morales-Ruiz, V. Puntes, W. Jiménez, Cerium oxide nanoparticles: a new therapeutic tool in liver diseases, Antioxidants. 10 (2021) 660–1623, https://doi.org/10.3390/antiox10050660.

[24] N.M. Zholobak, V.K. Ivanov, A.B. Shcherbakov, Chapter 12 - Interaction of nanoceria with microorganisms, in: Nanobiomaterials in antimicrobial therapy, William Andrew Publishing, 2016, pp. 419–450, https://doi.org/10.1016/B978-0-323-42864-4.00012-9.

[25] L.P. Babenko, N.M. Zholobak, A.B. Shcherbakov, S.I. Voychuk, L.M. Lazarenko, M. Y. Spivak, Antibacterial activity of cerium colloids against opportunistic microorganisms in vitro, Mikrobiol. Z. 74 (2012) 54–62, PMID:22830198. https://pubmed.ncbi.nlm.nih.gov/22830198/.

[26] I.A.P. Farias, C.C.L. Santos, A.L. Xavier, T.M. Batista, Y.M. Nascimento, J.M.F. F. Nunes, P.M.F. Silva, R.A. Menezes-Júnior, J.M. Ferreira, E.O. Lima, J.F. Tavares, M.V. Sobral, D. Keyson, F.C. Sampaio, Synthesis, physicochemical characterization, antifungal activity and toxicological features of cerium oxide nanoparticles, Arab. J. Chem. 14 (2021), 102888, https://doi.org/10.1016/j.arabjc.2020.10.035.

[27] N.M. Zholobak, Z.M. Olevinskaia, N.I. Spivak, A.B. Shcherbakov, V.K. Ivanov, A.V. Usatenko, Antiviral effect of cerium dioxide nanoparticles stabilized by low-molecular polyacrylic acid, Mikrobiolohichnyi Zhurnal (Ukraine). 72 (2010) 42–47, PMID: 20695228. https://pubmed.ncbi.nlm.nih.gov/20695228/.

[28] O. Shydlovska, E. Kharchenko, I. Osenniy, M. Spivak, A. Shcherbakov, N. Zholobak, Nanoparticles of cerium dioxide – an effective antiviral agent and adjuvant of biologically active molecules, ScienceRise: Biological Science 1 (2018) 26–30, https://doi.org/10.15587/2519-8025.2018.124686. http://journals.uran.ua/sr_bio/article/view/124686.

[29] N.M. Zholobak, A.B. Shcherbakov, E.O. Vitukova, A.V. Yegorova, Y.V. Scripinets, I. I. Leonenko, A.Y. Baranchikov, V.P. Antonovich, V.K. Ivanov, Direct monitoring of the interaction between ROS and cerium dioxide nanoparticles in living cells, RSC Adv. 4 (2014) 51703–51710, https://doi.org/10.1039/C4RA08292C.

[30] H.E.A. Mohamed, S. Afridi, A.T. Khalil, M. Ali, T. Zohra, R. Akhtar, A. Ikram, Z. K. Shinwari, M. Maaza, Promising antiviral, antimicrobial and therapeutic

[31] P. Allawadhi, A. Khurana, S. Allwadhi, K. Joshi, G. Packirisamy, K.K. Bharani, Nanoceria as a possible agent for the management of COVID-19, Nano Today. 35 (2020), 100982, https://doi.org/10.1016/j.nantod.2020.100982.

[32] A. Nefedova, K. Rausalu, E. Zusinaite, A. Vanetsev, M. Rosenberg, K. Koppel, S. Lilla, M. Visnapuu, K. Smits, V. Kisand, T. Tätte, A. Ivask, Antiviral efficacy of cerium oxide nanoparticles, Sci. Rep. 12 (2022) 18746, https://doi.org/10.1038/s41598-022-23465-6.

[33] N.M. Zholobak, A.P. Mironenko, A.B. Shcherbakov, O.A. Shydlovska, M.Y. Spivak, L.V. Radchenko, A.I. Marinin, O.S. Ivanova, A.E. Baranchikov, V.K. Ivanov, Cerium dioxide nanoparticles increase immunogenicity of the influenza vaccine, Antiviral Res. 127 (2016) 1–9, https://doi.org/10.1016/j.antiviral.2015.12.013.

[34] J.M. White, G.R. Whittaker, Fusion of enveloped viruses in endosomes, Traffic. 17 (2016) 593–614, https://doi.org/10.1111/tra.12389.

[35] S. Roche, A.A.V. Albertini, J. Lepault, S. Bressanelli, Y. Gaudin, Structures of vesicular stomatitis virus glycoprotein: membrane fusion revisited, Cell. Mol. Life Sci. 65 (2008) 1716–1728, https://doi.org/10.1007/s00018-008-7534-3.

[36] T. Kampmann, D.S. Mueller, A.E. Mark, P.R. Young, B. Kobe, The role of histidine residues in low-pH-mediated viral membrane fusion, Structure 14 (2006) 1481–1487, https://doi.org/10.1016/j.str.2006.07.011.

[37] A.B. Shcherbakov, N.M. Zholobak, N.Y. Spivak, V.K. Ivanov, Advances and prospects of using nanocrystalline ceria in cancer theranostics, Russ. J. Inorg. Chem. 59 (2014) 1556–1575, https://doi.org/10.1134/S003602361413004X.

[38] X. Sun, V.K. Yau, B.J. Briggs, G.R. Whittaker, Role of clathrin-mediated endocytosis during vesicular stomatitis virus entry into host cells, Virology. 338 (2005) 53–60, https://doi.org/10.1016/j.virol.2005.05.006.

[39] S. Singh, A. Kumar, A. Karakoti, S. Seal, W.T. Self, Unveiling the mechanism of uptake and sub-cellular distribution of cerium oxide nanoparticles, Mol. Biosyst. 6 (2010) 1813–1820, https://doi.org/10.1039/C0MB00014K.

[40] J. Mazzolini, R.J.M. Weber, H.-S. Chen, A. Khan, E. Guggenheim, R.K. Shaw, J. K. Chipman, M.R. Viant, J.Z. Rappoport, Protein corona modulates uptake and toxicity of nanoceria via clathrin-mediated endocytosis, Biol. Bull. 231 (2016) 40–60, https://doi.org/10.1086/689590.

[41] A.T. Da Poian, F.A. Carneiro, F. Stauffer, Viral inactivation based on Inhibition of membrane fusion: understanding the role of histidine protonation to develop new viral vaccines, Protein Pept. Lett. 16 (2009) 779, https://doi.org/10.2174/092986609788681823.

[42] M. Mogensen, N.M. Sammes, G.A. Tompsett, Physical, chemical and electrochemical properties of pure and doped ceria, Solid State Ionics. 129 (2000) 63–94, https://doi.org/10.1016/S0167-2738(99)00318-5.

[43] N. Tsud, R.G. Acres, M. Iakhnenko, D. Mazur, K.C. Prince, V. Matolín, Bonding of histidine to cerium oxide, J. Phys. Chem. B. 117 (2013) 9182–9193, https://doi.org/10.1021/jp404385h.

[44] S. Bercha, K. Beranová, R.G. Acres, M. Vorokhta, M. Dubau, I. Matolínová, T. Skála, K.C. Prince, V. Matolín, N. Tsud, Thermally controlled bonding of adenine to cerium oxide: effect of substrate stoichiometry, morphology, composition, and molecular deposition technique, J. Phys. Chem. C. 121 (2017) 25118–25131, https://doi.org/10.1021/acs.jpcc.7b06925.

[45] A. Almutary, B.J.S. Sanderson, The MTT and crystal violet assays: potential confounders in nanoparticle toxicity testing, Int. J. Toxicol. 35 (2016) 454–462, https://doi.org/10.1177/1091581816648906.

[46] L. Śliwka, K. Wiktorska, P. Suchocki, M. Milczarek, S. Mielczarek, K. Lubelska, T. Cierpiał, P. Łyzwa, P. Kiełbasiński, A. Jaromin, A. Flis, Z. Chilmonczyk, The comparison of MTT and CVS assays for the assessment of anticancer agent interactions, PLoS One. 11 (2016) 1–17, https://doi.org/10.1371/journal.pone.0155772.

[47] A.R. Fehr, S. Perlman, in: Coronaviruses: an overview of their replication and pathogenesis, Methods Mol. Biol. 1282, 2015, pp. 1–23, https://doi.org/10.1007/978-1-4939-2438-7_1.

[48] A.V. Nicola, S.E. Straus, Cellular and viral requirements for rapid endocytic entry of herpes simplex virus, J. Virol. 78 (2004) 7508–7517, https://doi.org/10.1128/jvi.78.14.7508-7517.2004.

[49] N.M. Zholobak, A.B. Shcherbakov, A.S. Bogorad-Kobelska, O.S. Ivanova, A. Y. Baranchikov, N.Y. Spivak, V.K. Ivanov, Panthenol-stabilized cerium dioxide nanoparticles for cosmeceutic formulations against ROS-induced and UV-induced damage, J. Photochem. Photobiol. B Biol. 130 (2014) 102–108, https://doi.org/10.1016/j.jphotobiol.2013.10.015.

[50] F. Zhang, S.-W. Chan, J.E. Spanier, E. Apak, Q. Jin, R.D. Robinson, I.P. Herman, Cerium oxide nanoparticles: Size-selective formation and structure analysis, Appl. Phys. Lett. 80 (2002) 127–129, https://doi.org/10.1063/1.1430502.

[51] S. Tsunekawa, T. Fukuda, A. Kasuya, Blue shift in ultraviolet absorption spectra of monodisperse CeO_{2-x} nanoparticles, J. Appl. Phys. 87 (2000) 1318–1321, https://doi.org/10.1063/1.372016.

[52] S.V.N.T. Kuchibhatla, A.S. Karakoti, S. Thevuthasan, S. Seal, D.R. Baer, Influence of aging on the properties of cerium oxide nanoparticles - implications to quantum confinement effect, in: 11th IEEE Int. Conf. Nanotechnol., 2011: pp. 646–650, doi: 10.1109/NANO.2011.6144639. https://ieeexplore.ieee.org/document/6144639.

[53] N.S. Arul, D. Mangalaraj, P.C. Chen, N. Ponpandian, C. Viswanathan, Strong quantum confinement effect in nanocrystalline cerium oxide, Mater. Lett. 65 (2011) 2635–2638, https://doi.org/10.1016/j.matlet.2011.05.022.

[54] J.C. Nie, Z.Y. Hua, R.F. Dou, Q.Y. Tu, Quantum confinement effect in high quality nanostructured CeO_2 thin films, J. Appl. Phys. 103 (2008) 54308, https://doi.org/10.1063/1.2841719.

[55] G.A. Parks, The Isoelectric Points of Solid Oxides, Solid Hydroxides, and Aqueous Hydroxo Complex Systems, Chem. Rev. 65 (1965) 177–198, https://doi.org/10.1021/cr60234a002.

[56] T. Skála, F. Šutara, K.C. Prince, V. Matolín, Cerium oxide stoichiometry alteration via Sn deposition: Influence of temperature, J. Electron Spectros. Relat. Phenomena. 169 (2009) 20–25, https://doi.org/10.1016/j.elspec.2008.10.003.

[57] S. Tanuma, C.J. Powell, D.R. Penn, Calculations of electron inelastic mean free paths (IMFPS). IV. Evaluation of calculated IMFPs and of the predictive IMFP formula TPP-2 for electron energies between 50 and 2000 eV, Surf. Interface Anal. 20 (1993) 77–89, https://doi.org/10.1002/sia.740200112.

[58] S. Bercha, G. Mali, I. Khalakhan, T. Skála, K.C. Prince, V. Matolín, N. Tsud, Histidine adsorption on nanostructured cerium oxide, J. Electron Spectros. Relat. Phenomena. 212 (2016) 28–33, https://doi.org/10.1016/j.elspec.2016.07.005.

[59] Y. Kosto, Study of cerium oxide thin films for biosensing applications, Charles University, 2021. https://dspace.cuni.cz/handle/20.500.11956/125397. Doctoral Thesis.

[60] N. Tsud, S. Bercha, R.G. Acres, M. Vorokhta, I. Khalakhan, K.C. Prince, V. Matolin, Functionalization of nanostructured cerium oxide films with histidine, Phys. Chem. Chem. Phys. 17 (2015) 2770–2777, https://doi.org/10.1039/C4CP03780D.

[61] Y. Kosto, G. Barcaro, V. Kalinovych, S. Franchi, P. Matvija, I. Matolínová, K. C. Prince, V. Matolín, T. Skála, N. Tsud, V. Carravetta, Role of the redox state of cerium oxide on glycine adsorption: an experimental and theoretical study, Phys. Chem. Chem. Phys. 25 (2023) 6693–6706, https://doi.org/10.1039/D2CP06068J.

[62] L. Wu, H.J. Wiesmann, A.R. Moodenbaugh, R.F. Klie, Y. Zhu, D.O. Welch, M. Suenaga, Oxidation state and lattice expansion of CeO_{2-x} nanoparticles as a function of particle size, Phys. Rev. B. 69 (2004) 1254151–1254159, https://doi.org/10.1103/PhysRevB.69.125415.

[63] D.R. Mullins, S.H. Overbury, D.R. Huntley, Electron spectroscopy of single crystal and polycrystalline cerium oxide surfaces, Surf. Sci. 409 (1998) 307–319, https://doi.org/10.1016/S0039-6028(98)00257-X.

[64] C. Zhang, T. Zhang, J. Zou, C.L. Miller, R. Gorkhali, J.-Y. Yang, A. Schilmiller, S. Wang, K. Huang, E.M. Brown, K.W. Moremen, J. Hu, J.J. Yang, Structural basis for regulation of human calcium-sensing receptor by magnesium ions and an unexpected tryptophan derivative co-agonist, Sci. Adv. 2 (2016) e1600241, doi: 10.1126/sciadv.1600241. https://www.science.org/doi/10.1126/sciadv.1600241.

[65] J. Henych, M. Šťastný, J. Ederer, Z. Němečková, A. Pogorzelska, J. Tolasz, M. Kormunda, P. Ryšánek, B. Bażanów, D. Stygar, K. Mazanec, P. Janoš, How the surface chemical properties of nanoceria are related to its enzyme-like, antiviral and degradation activity, Environ. Sci. Nano. 9 (2022) 3485–3501, https://doi.org/10.1039/D2EN00173J.

[66] C.J. Neal, C.R. Fox, T.S. Sakthivel, U. Kumar, Y. Fu, C. Drake, G.D. Parks, S. Seal, Metal-mediated nanoscale cerium oxide inactivates human coronavirus and rhinovirus by surface disruption, ACS Nano. 15 (2021) 14544–14556, https://doi.org/10.1021/acsnano.1c04142.

[67] D.C. Johnson, M. Webb, T.W. Wisner, C. Brunetti, Herpes simplex virus gE/gI sorts nascent virions to epithelial cell junctions, promoting virus spread, J. Virol. 75 (2001) 821–833, https://doi.org/10.1128/JVI.75.2.821-833.2001.

[68] D.S. Mueller, T. Kampmann, R. Yennamalli, P.R. Young, B. Kobe, A.E. Mark, Histidine protonation and the activation of viral fusion proteins, Biochem. Soc. Trans. 36 (2008) 43–45, https://doi.org/10.1042/BST0360043.

[69] T. Tang, M. Bidon, J.A. Jaimes, G.R. Whittaker, S. Daniel, Coronavirus membrane fusion mechanism offers a potential target for antiviral development, Antiviral Res. 178 (2020) 104792, https://doi.org/10.1016/j.antiviral.2020.104792.

[70] P.G. Spear, R. Longnecker, Herpesvirus entry: an update, J. Virol. 77 (2003) 10179–10185, https://doi.org/10.1128/JVI.77.19.10179-10185.2003.

[71] C. Feng, P. Fang, Y. Zhou, L. Liu, L. Fang, S. Xiao, J. Liang, Different effects of His-Au NCs and MES-Au NCs on the propagation of pseudorabies virus, Glob. Challenges. 2 (2018) 1800030, https://doi.org/10.1002/gch2.201800030.

[72] F.A. Carneiro, P.A. Lapido-Loureiro, S.M. Cordo, F. Stauffer, G. Weissmüller, M. L. Bianconi, M.A. Juliano, L. Juliano, P.M. Bisch, A.T.D. Poian, Probing the interaction between vesicular stomatitis virus and phosphatidylserine, Eur. Biophys. J. 35 (2006) 145–154, https://doi.org/10.1007/s00249-005-0012-z.

[73] F.A. Carneiro, F. Stauffer, C.S. Lima, M.A. Juliano, L. Juliano, A.T. Da Poian, Membrane fusion induced by vesicular stomatitis virus depends on histidine protonation, J. Biol. Chem. 278 (2003) 13789–13794, https://doi.org/10.1074/jbc.M210615200.